EUROPEAN ORGANIZATION FOR NUCLEAR RESEARCH
European Laboratory for Particle Physics

STUDY OF THE SURFACE RESISTANCE OF SUPERCONDUCTING NIOBIUM FILMS AT 1.5 GHz

C. Benvenuti, S. Calatroni, I.E. Campisi [1], P. Darriulat,
M.A. Peck, R. Russo [2] and A.-M. Valente

Abstract

A systematic study of superconducting properties of niobium films sputtered on the inner wall of radiofrequency cavities is presented. The measured quantities include in particular the response to 1.5 GHz microwaves, the critical temperature, the penetration depth and the magnetic penetration field. In addition to films grown in different gas discharges (Xe, Kr, Ar and Ar/Ne mixtures) and to films grown on substrates prepared under different conditions, the study includes also bulk niobium cavities. The surface resistance is analysed in terms of its dependence on temperature, on RF field and, when relevant, on the density of trapped fluxons. A simple parameterisation is found to give a good fit to the data. Once allowance for the presence of impurities and defects is made by means of a single parameter, the electron mean free path, good agreement with BCS theory is observed. The fluxon-induced losses are studied in detail and their dependence on RF field, on temperature and on the density of trapped fluxons is analysed. The residual resistance is observed to be essentially uncorrelated with the other variables, suggesting that it is dominantly extragranular. In occasions very low residual resistances, in the $n\Omega$ range, have been maintained over a broad range of RF field, indicating the absence of significant fundamental limitations specific to the film technology in practical applications such as the production of accelerating cavities for particle accelerators.

Submitted for publication in PHYSICA C

Geneva, Switzerland
September 1998

1) *Scientific Associate on leave from TJNAF, Newport News, Virginia, USA*
2) *Present address: Dip. di Sc. Fis. and INFM, U. degli Studi di Salerno,84081 Baronissi, Italy*

1. Introduction

The response of a superconductor to an incident electromagnetic wave has been the object of intense research for many years. It has been calculated in the framework of the BCS theory [1] by Mattis and Bardeen [2] and independently by Abrikosov, Gor'kov and Khalatnikov [3] as early as 1958. Much of the experimental work has been driven by applications to the fields of fast electronics and particle accelerators [4]. In the latter case, most of the attention has been given to the development of superconducting RF cavities, operated in the 0.1 to 5 GHz range, and producing as large as possible an electric field along their axis, typically in the 10 MV/m range. While such cavities are usually made of bulk niobium, the recent successful operation [5] of LEP2 at CERN has demonstrated the feasibility of using instead high purity copper cavities, the inner walls of which are covered by a thin superconducting niobium film [6]. The aim of the present work is to improve our understanding of the physics phenomena governing the response of such films to microwaves.

The experimental method consists in coating the inner wall of copper resonators with niobium films of different purity and structural properties and in measuring the dependence of their surface resistance upon various parameters: temperature, amplitude of the incident wave, purity and structural properties of the film, and, in the case where fluxons have been trapped, density of their lattice. Such a program implies a large number of independent series of measurements, each time using a different film, in order to secure the consistency of the data. In practice a same resonator is re-used several times, serving as a substrate to different films in sequence, the new film being deposited onto the chemically refreshed copper surface once the preceding film has been removed. For such a procedure to remain manageable, it is important to keep the size of the resonators such that they can be handled easily in the course of the many successive operations that are necessary for each cycle. This constraint influenced the choice of 1.5 GHz as resonance frequency, resulting in a cell length of 10 cm and diameter of 18 cm for operation in the fundamental TM_{010} mode (Fig. 1). This frequency is much lower than the critical frequency ($\sim$ 740 GHz) above which the energy of the incident photons is sufficient to break the Cooper pairs. While it is about four times higher than the frequency of the LEP2 resonators, it is nearly equal to that used in other existing or planned accelerators such as CEBAF [7] and TESLA [8].

The use of a resonator to study superconducting properties has the advantage of offering clean operating conditions for the RF measurement with an excellent sensitivity to small effects, typically down to a few nΩ. However, its relatively large area ($\sim$ 670 cm^2) implies numerous inhomogeneities, which must be averaged over when analysing the data. These include the distributions of the microwave amplitude, of the temperature, of the density of trapped fluxons and of possible surface defects.

A particularity of the present work is the systematic use which is made of trapped fluxons [9] to obtain specific information on the impurities and defects which act as pinning centres in the superconductor. This is studied by cooling down the resonator below critical temperature (T_c) in the presence of a uniform magnetic field of a few Gauss, parallel to the cavity axis. In most cases the films are observed to strongly pin the fluxon lattice, thereby preventing their expulsion by Meissner effect. The additional surface resistance induced by such fluxons gives information on the nature and density of the pinning centres. At the same time the normal conducting fluxon cores provide a controlled source of RF losses that can serve as a reference in the comparison with other possible sources.

The paper is organised as follows: Section 2 introduces the surface resistance of superconductors, its expression as a function of various quantities and a parameterisation allowing for a convenient interpretation of the data. Section 3 gives a brief summary of the experimental method and techniques used in the various steps of the study. Section 4 describes the method used in data analysis, taking as an example the measurements associated with a particular type of film. Section 5 summarises the results obtained for different films, comparing them with those of bulk niobium data. A global discussion of the results and some concluding remarks are presented in Section 6.

2. The surface resistance of superconductors

The response of a superconductor to an incident microwave is described in terms of its complex surface impedance, $Z_s = R_s + iX_s$, equal to the ratio between the complex amplitudes, E_{rf} and H_{rf} of the electric and magnetic components of the field in the superconductor near its surface. The surface resistance R_s is related to the power P absorbed in the superconductor per unit area,

$$P = 1/2 \, R_s \, H_{rf}^{\,2} \tag{1}$$

and the surface reactance X_s is a direct measure of the penetration depth λ of the field inside the superconductor.

The use of the BCS formalism to describe the pair condensation mechanism, neglecting any possible dependence of the zero temperature energy gap Δ on the momentum of the exchanged phonon, allows for a straightforward calculation [2, 3] of the surface resistance as a function of temperature T, of the microwave angular frequency ω and of the various parameters describing the superconductor (including a mean free path l that accounts for the possible presence of extraneous scattering centres). The results take the form of integrals which cannot be reduced to an analytical form, but need to be calculated numerically [10]. However for temperatures sufficiently lower than T_c, a form

$$R_s = R_{BCS} \propto \frac{1}{T} \exp\left(\frac{-\Delta}{T}\right) \tag{2}$$

gives a fair approximation to the exact result and provides a convenient tool for a simple interpretation of experimental data.

The surface resistance R_{BCS}, referred to as the BCS resistance, is dominated by the interactions of the unpaired conduction electrons and vanishes at $T = 0$ where they have all condensed into Cooper pairs. Several authors [11] have discussed the validity of the approximations made in Ref. 2 and 3 and concluded that they should induce only small corrections for the range of parameters relevant to the present work. In particular strong coupling can be taken into account by simply allowing $\alpha = \Delta/T_c$ to depart from its standard BCS value, $\alpha_{BCS} = 1.76$. A review of the current status of the theory and of its description of the superconducting properties of niobium is available in Ref. 12.

The limitation to first order in the field of the perturbative expansion used in the calculations of Ref. 2 and 3 implies that R_{BCS} is independent of the microwave amplitude, in contradiction with experimental observation. The use of a perturbative expansion in the

pair potential leads instead to the Ginzburg-Landau equations, with the critical fields $H_{c1} < H_c < H_{c2}$ giving the scale of the H_{rf} dependence of the surface resistance [13]. It is common practice [14] to identify R_{BCS} with its value at $H_{rf} = 0$ and to assume factorisation of the H_{rf} dependence, a practice that is followed in the present work. The data at $H_{rf} = 0$ will be compared with theory and their evolution with H_{rf} will be described by an *ad hoc* parameterisation.

Rather than vanishing together with T the surface resistance is experimentally observed to level off at a value R_{res}, the residual surface resistance, resulting from the presence of impurities and defects in the sample [15]. It is commonly assumed that R_{res} is temperature independent in the range $T \ll T_c$, an assumption that is supported by experimental observation. In the present work most measurements extend down to $T = 1.7$ K where R_{BCS} has become very small, thereby providing an unambiguous separation of the two terms.

While losses described by R_{BCS} are distributed over the whole sample, additional losses induced by the presence of trapped fluxons are localised in the neighbourhood of pinning centres and are described in terms of an additional resistance R_{fl}. Phenomenological descriptions of the various factors contributing to fluxon-induced losses can be found in the literature [16] but most of these focus on the dc regime, and very few authors discuss the case of strongly pinned fluxons in a low external field H_{ext} and a moderately strong RF field, the situation of relevance to most of the present work. Moreover they usually consider a linear regime with R_{fl} of the present experiment. For the time being it is therefore sufficient to expand Relation 2 into independent from the microwave amplitude, a situation in sharp disagreement with the results

$$R_s (H_{rf}, H_{ext}, T) = R_{BCS} (H_{rf}, T) + R_{res} (H_{rf}) + R_{fl} (H_{rf}, H_{ext}, T). \qquad (3)$$

Further comments on the form taken by R_{fl} and on its dependence on H_{ext}, H_{rf} and T can await a comparison with experimental data.

3. Experimental method and procedure

3.1 Preparation and characterisation of the substrate

The resonators consist of an axially symmetric cell having a nearly elliptical profile optimised for RF excitation of the fundamental 1.5 GHz TM_{010} mode and for prevention of multipacting [17]. The geometry of the cavity and the distribution of the amplitudes of the electric and magnetic fields on the cavity surface are shown in Fig. 1. The magnetic field amplitude reaches a flat maximum at the equator and remains above 80% of its maximal value over 80% of the cell area, decreasing to 20% of its maximal value at the iris. In the present work we neglect this variation, as well as the variation of the film characteristics over the cell surface and always refer to H_{rf} as its mean value, properly averaged over the cell area. The electric field is instead maximal at the iris and vanishes at the equator. As a consequence, defects and impurities located in the equatorial region influence preferentially the surface resistance, while those located near the iris are potential sources of field emission, limiting the amount of RF energy that can be safely stored in the cavity [18]. The data presented in this study are restricted to a field range from which such effects are absent, leaving the study of field emission and of its influence on the RF response to a later publication.

The cavity walls, serving as a substrate for the deposition of the niobium film, are made of high purity copper in order to minimise the temperature gradient across the walls during RF operation, while maintaining a sufficient mechanical rigidity. Several processes have been used to manufacture the cavities, namely hydroforming, lathe spinning and electroforming. Hydroformed cavities are made starting from oxygen free electronic grade (OFE) tubes inflated at high pressure inside a mandrel in three successive steps, each preceded by a vacuum annealing at 600°C for one hour [19]. Spun cavities are made starting from 3 mm thick OFE sheets, previously vacuum annealed at 250°C for two hours, and shaped over a collapsible inner mandrel [20]. Electroformed cavities are made by the pulse plating technique [21] using a copper pyrophosphate bath and a metallized inner glass mandrel subsequently dissolved in hydrofluoric acid. In order to improve the thermal conductivity, an intermediate annealing is made at 500°C for two hours. All three manufacturing techniques have the advantage of avoiding the need for an equatorial weld, at variance with the more common technique of deep-drawing.

Prior to coating, the copper substrate is chemically polished in order to obtain a clean and smooth surface. For hydroformed cavities the removal of 40 μm is usually sufficient, whereas for spun cavities optical microscopy has indicated that at least 120 μm must be removed in order to eliminate the flaws generated by the spinning process. On electroformed cavities the initial polishing is of approximately 25 μm in order to remove the remnants of the chemical dissolution of the mandrel and the initial layer deposited under dc conditions without unduly affecting the smoothness of the surface. The polishing agent (SUBU) is a mixture of sulfamic acid, hydrogen peroxide, n-butanol and ammonium citrate [22]. For subsequent coatings, after having stripped the preceding niobium film with a solution containing hydrofluoric acid and sodium benzoate, the removal of 10 to 20 micrometers of copper is usually sufficient. Typically ten successive coatings can be made on a same substrate depending on the initial thickness, after which its mechanical rigidity may become too low for further use.

Chemicals are removed from the cavity surface by a 100 bar rinsing using at least one cubic meter of ultra-pure water under filtered nitrogen atmosphere. The resistivity of the output water is monitored. It stabilises at its input value, in excess of 17 MΩcm, after typically 500 litres.

The main relevant properties of the finished copper substrate have been investigated. The results obtained for typical samples, representative of the equatorial region of the cell for each of the three manufacturing processes and chemically polished as described above, are summarised in Table 1. A classical four leads method was used for the *RRR* measurements in liquid helium. Oxygen content analyses were made by outgassing at 950°C in helium and measuring the outgassed quantity by mass spectrometry, while other impurities were identified and their relative abundance measured using glow discharge optical emission spectroscopy (GDOS). The grain size was measured by optical microscopy and quantified with the help of an image analyser. The Vickers microhardness and the average roughness were measured using standard methods, the latter with a stylus having a tip diameter of ten micrometers.

In a few cases we have used bulk niobium cavities either to serve as a reference or as substrates for deposition of a niobium film. These were produced from high purity niobium sheets (nominal *RRR* ~ 300) either by spinning as described above or by electron welding of two deep-drawn half cells [23]. In order to suppress the damaged superficial layer, at least

120 µm were removed by buffered chemical polishing (BCP), using a standard solution of HF, HNO_3 and H_3PO_4, 1:1:1 in volume. The cavities could be subsequently heat-treated in successive steps, at temperatures ranging between 800 and 1100°C, in order to study the resulting evolution of their superconducting properties. The cavity to be treated was enclosed, together with test samples, in a niobium box, itself enclosed in a titanium box used as getter material. This design ensured an optimal gettering efficiency of the desorbed gases while protecting the cavity from the furnace residual pressure and preventing contamination of the cavity and test samples by titanium atoms. After each thermal cycle, the samples have been analysed in order to estimate the impurity level of the films and to obtain information about the evolution of the grain size and *RRR* value with temperature.

3.2 Niobium coating

The niobium films, typically 1.5 µm thick, are grown on the copper inner walls of the resonators by sputtering in a cylindrical magnetron configuration (Fig. 2), a low pressure gas discharge being established inside the resonator, ejecting niobium atoms from a high purity cathode located along its axis and projecting them onto its wall [24]. After assembly in a class 100 clean room, the cathode and the cavity to be coated are baked out at a temperature of 150°C for 20 hours. At the end of the operation the ultimate pressure is measured to reach typically 10^{-9} mbar, dominated by hydrogen.

The niobium cathode (*RRR* ~ 300) is a cylindrical tube 48 mm in diameter. A same cathode is used for about 30 coatings. Before the first operation it is BCP polished and conditioned in a preliminary coating run. The design of the cathode is the result of an optimisation of the uniformity of the film thickness over the cavity surface. Scanning electron microscopy (SEM) cross-section observations and surface density measurements made on samples cut from coated cavities show that the film thickness does not deviate by more than ± 10% from its average value. From the visible erosion of the cathode surface it is possible to infer the size of the active region, typically ± 1 cm along the cavity axis from its centre. Such a source size, when assuming a cosine law for the emission mechanism, implies mean incidence angles of the atoms on the cavity wall of typically 15 ± 5°, varying from 9 ± 4° at the equator to 50 ± 10° near the irises. Sample studies indicate that the incidence angle must be kept below 50° in order to ensure a good film quality.

The gas discharge is established in a noble gas atmosphere, usually argon, at a pressure of 1.5×10^{-3} mbar. A stable current of 3 A is set between the cathode and the grounded cavity wall, corresponding to a voltage of ~ 360 V. A permanent magnet, located inside the cathode, produces a field of about 100 G on its outer surface, resulting in an increase of the ionisation efficiency by approximately two orders of magnitude. The discharge voltage fixes the energy of the noble gas ions impinging on the niobium cathode and its power defines the sputtering rate. The kinetic energy distribution of the ejected niobium atoms does not depend appreciably on the discharge parameters.

Cavities are usually coated at 150°C, a compromise between lower temperatures causing a deterioration of the film purity and higher temperatures causing the copper substrate to become softer. The central cell and the extension tubes are coated in a single operation, the latter being coated first using slightly different discharge parameters. In order to remove the oxide layer from the cathode surface as early as possible over its whole length, a preliminary pre-cleaning is made by scanning the magnet back and forth over the whole cathode length

for about 9 mn, corresponding to a film thickness of ~ 50 nm in the central cell. Coating the central cell takes typically 15 mn for an average film thickness of 1.5 μm.

After coating, the cavity is vented to dry air as soon as the temperature of the system reaches room temperature. Oxidation of the surface by dry air favours the exclusive formation of a Nb_2O_5 layer [25], while venting to wet air might result in an uncontrolled formation of other compounds, in particular hydroxides. After assembly of the end flanges the cavity is rinsed with high pressure water (as described in Section 3.1) and dry pumped at 60°C before being installed in the cryostat where its surface resistance and other superconductivity variables are measured.

The coating procedure described above implies the presence of an oxide layer at the interface between the copper substrate and the niobium film. A second coating system, making it possible to eliminate this oxide layer before growing the niobium film, has been used to study its effect. It includes two separate electrodes, which can be introduced independently from either side of the cavity along its axis from chambers where they are stored under UHV conditions when not in use. The first electrode is made of copper and used as an anode to reverse-sputter out from the cavity surface whatever impurities may be present over a depth of approximately 50 nm. Special care is required to maintain stable discharge conditions in this geometry. The desorbed gases are pumped out and analysed in order to monitor the progress of the cleaning process. An ion dose of approximately 2×10^{18} ions/cm^2 is found to be sufficient for an effective cleaning. By then the gas contamination has decreased by nearly two orders of magnitude. The copper anode is then replaced by the niobium cathode (which does not need to be pre-cleaned any longer) and coating proceeds as described earlier. As a consistency check of the coherence of the results obtained with each of the two coating systems, a few films have been grown in the second system after having let it cool down and having vented it to filtered air after the reverse-sputtering phase, thus re-establishing the oxide layer at the copper-niobium interface.

3.3 Structural properties and impurity content of the film

The structural properties and impurity content of the niobium films were studied on samples cut from previously measured cavities or from samples prepared under similar conditions as the cavities. In the former case the superconducting properties measured at low temperature are exactly known but the sample curvature limits the accuracy of some of the measurements. The latter are more suitable for accurate measurements and do not require the destruction of a cavity. However their RF superconducting properties are not directly available and must be estimated using data obtained from cavities prepared under similar conditions.

Samples have been analysed by X-ray diffraction (XRD) in the Bragg-Brentano configuration. Spectra measured on samples cut from the equatorial region show that the films grow with a pronounced texture, the (110) plane being preferentially parallel to the surface (see Section 6.4). Flat samples are necessary for the study of the stress induced in the film by the growth process and for the measurement of the texture [26]. For films grown at 150°C an increase of the lattice parameter of $0.64 \pm 0.06\%$ of the bulk value is observed. The stress caused by the different thermal expansion coefficients of niobium and copper accounts for approximately 0.1%. The elastic stresses of the film can be released by dissolving the copper substrate in a nitric acid solution, thus restoring the lattice parameter and the critical temperature to their bulk values.

The *RRR* value and the contamination by atoms of the discharge gas have been measured on flat films grown on quartz substrates (Table 2), the xenon and krypton discharges requiring a higher voltage (~ 600 V). The method used in the latter case takes advantage of the existence of a niobium-nickel eutectic which melts at 1175°C: the film, in contact with a nickel foil of high purity is heated in a UHV furnace and the amount of gas released during melting is measured. The relative accuracy is ~ 20% and the sensitivity limit is ~ 5 ppm. The method allows also for an evaluation of the hydrogen concentration in the film by integrating the total quantity released throughout the whole heating cycle. It is typically measured at the level of a few atomic permil. Other contaminants, such as carbon and oxygen, were searched for using secondary ion mass spectroscopy (SIMS) and do not exceed 100 ppm. Transmission electron microscopy (TEM) and SEM analyses were performed in order to obtain information on topological defects and on the grain size. TEM pictures show a columnar grain structure of the films with an average grain diameter of 200 ± 50 nm for standard films. Defects in the film are observed to have their origin in defects of the substrate and/or in possible contaminants present on the copper surface prior to niobium deposition.

Finally, AES measurements have been performed in order to estimate the thickness of the oxide layer on the niobium surface. The measurements are affected by the value of the surface roughness but the layer thickness can be estimated to be somewhere between 2 and 6 nm.

3.4 Measurement of the surface resistance

Once it has been coated and rinsed the cavity under study is evacuated and installed in a liquid helium cryostat where the temperature can be lowered down to 1.5 K. Two cylindrical antennas connected to 50 Ω ceramic feedthroughs, one on each of the end flanges, couple the cavity to the external circuit via coaxial cables. The length of the input antenna is adjusted to keep the coupling within a factor 10 of its critical value over the whole range and, for each measurement, the incident phase is tuned manually to minimise reflection. An oscillator is used to generate an RF signal of power adjustable between 0 and 20 mW which is then amplified in a travelling wave tube amplifier having a gain of 40 dB. The transmitted signal is used to lock the oscillator on the resonance frequency of the cavity. It is capacitively coupled in order to allow for a measurement with a sensitivity of ~ 10 pA of a possible dc current, typically in the nA range, signalling the collection of field emitted electrons by the output antenna. An X-ray counter, located on top of the cryostat on the cavity axis, provides an independent detection of field emission.

The incident, reflected and transmitted powers, P_i, P_r and P_t, are probed with 20 dB directional couplers and measured using a spectrum analyser. An independent measurement using bolometric powermeters serves as a consistency check. The power dissipated in the cavity wall, $P_c = P_I - P_r - P_t$, is deduced from this measurement. Computer control of the whole system allows for on-line monitoring, detection of possible malfunctions and frequent calibrations of the circuit parameters. In particular the decay time and the input and output couplings are measured at regular intervals by analysing the reflected signal on the input line when the incident power is switched on and off in succession, thus providing a calibration of the parameters defining the external circuitry. The quality factor, Q, is calculated from the measured powers after correction for the contributions of the external circuitry and the electric field gradient along the cavity axis, E_{acc}, is obtained from the relation $E^2_{acc}/(Q\,P_c) = 8.27$ kΩ/m^2, a constant depending exclusively on the shape and dimensions of the cavity.

A series of measurements of Q and E_{acc} is performed for different values of the temperature and of the incident input power (Fig. 3). The data are recorded for subsequent off-line analysis, together with other parameters of relevance including temperatures measured by thermometers in thermal contact with the cavity external wall at the equator and near each of the irises. They are then processed off-line using optimised circuit parameters, and measurement errors are evaluated and propagated through the various steps of the calculation. As a result, a series of measurements of the surface resistance, R_s, of the average RF magnetic field, H_{rf}, of the average temperature, T, and of their respective uncertainties are obtained. Here R_s is simply related to Q via the relation $R_s = G/Q$, where $G = 295 \ \Omega$ is a parameter depending exclusively on the shape of the cavity, while H_{rf} is related to E_{acc} via the relation H_{rf} (mT) $= 4.55 \ E_{acc}$ (MV/m). Here, we follow the tradition of expressing the RF field in mT and external static fields in G (c.g.s. units are used otherwise). The temperature is a weighted average of the thermometer measurements corrected for the temperature gradient across the cavity wall, its uncertainty includes their rms deviations with respect to the mean.

3.5 Flux trapping

For each cavity the series of measurements described in the previous subsection are repeated in several cycles, each time with a different value of the trapped magnetic flux. Flux trapping is achieved with the help of a solenoidal coil wound around the cryostat and producing a magnetic field parallel to the cavity axis and uniform over its volume. The coil is surrounded by a μ-metal cylinder shielding the cryostat from the earth field to better than 0.01 G. Care has been taken to prevent the presence of ferromagnetic material inside the cryostat. In practice each cycle implies draining the cryostat and letting the cavity temperature increase above T_c, to typically 15 K, switching the solenoid on at the desired field level H_{ext}, adjustable between 0 and 9 G, and refilling the cryostat with liquid helium.

Hall probes distributed along an outer meridian of the resonator are used to measure the normal magnetic field component in the vicinity of the superconductor's surface. As the cavity is cooled down below T_c, it crosses the transition from normal state to mixed phase when the temperature T is such that $H_{c2}(T) = H_{ext}$. At that time the magnetic flux condenses into a fluxon lattice having a density of $4.8 \times 10^4 \ \text{mm}^{-2}$ per Gauss of H_{ext}, too large for the effect to be detected on the 5 mm^2 area of each of the Hall probes. When the temperature decreases further and enters the Meissner phase, the Hall probe signal will remain unchanged if the flux is fully trapped, as is usually the case. If instead the flux is partly or completely expelled the Hall probe signal will be affected. For each cavity the field discontinuity ΔH detected by each of the Hall probes (with the solenoid on) when crossing the transition upwards is measured in two different configurations, one (ΔH_{on}) when the cavity had been cooled down in $H_{ext} \neq 0$, the other (ΔH_{off}) when the cavity had been cooled down in $H_{ext} = 0$. The parameter $\varepsilon = \Delta H_{on}/\Delta H_{off}$ measures the fraction of magnetic flux expelled from the film as it becomes superconducting. When the flux is fully trapped, $\varepsilon = 0$. However, as the Hall probes see only a very small fraction of the cavity area, the extrapolation of this result to the whole surface is only valid if the film is sufficiently homogeneous. In practice other features give confidence that this is indeed the case. When ε is measured to deviate from 0, a situation observed in the case of heat-treated bulk niobium cavities, it is only possible to conclude that a change in fluxon density occurred over the cavity area covered by the Hall probes. It is however not possible in this case to reliably deduce from the measurement of ε the value of the flux trapping efficiency averaged over the whole cavity area. Examples of such measurements are illustrated in Fig. 4. The accuracy of the ε measurement is about 1%.

As a by-product, the jump of ΔH_{off} across T_c provides a measurement of the critical temperature, the width of the transition being only slightly affected by the temperature gradient between the upper and lower parts of the resonator, which is kept below 4 mKcm^{-1} over the cavity length.

Moreover, tracking the cavity resonance frequency f when T approaches T_c provides a direct measurement of the temperature dependence of the penetration depth [27], $\lambda(T) = \lambda(0) F(t)$ with $\lambda(0) = \lambda_0 (1 + 0.5\pi \xi_0/l)^{0.5}$ and $t = T/T_c$, the reduced temperature. This measurement requires some care in ensuring that the resonance frequency is not significantly affected by extraneous parameters such as the helium gas pressure in the cryostat or the RF energy stored in the resonator. To the extent that F is a universal function and that identical experimental conditions are realised for each resonator, it provides a reliable relative measurement of the penetration depth. In practice the values of $\lambda(0)$ are obtained from a global fit of all the measured rates of increase of the resonant frequencies as a function of reduced temperature to a form $df/dt \propto \lambda(0) g(t)/(1-t)$. The universal function $g(t) = (1-t) dF/dt$ obtained this way, arbitrarily set equal to unity at $t = 0.9$, is displayed in Fig. 5. Its t dependence is very close to the prediction of the two-fluid model, $F(t) \propto (1-t^4)^{-0.5}$. When compared with BCS theory, the data allow for a crude evaluation of the London penetration depth, $\lambda_L(0) = 33 \pm 4$ nm.

During part of the experiment a small superconducting coil was attached to the external resonator wall at the equator and used to obtain a relative measurement of H_p, the magnetic penetration field. It can produce a field of up to 20 kG on the film surface. When applied on a cavity cooled down in $H_{ext} = 0$ (perfect Meissner state) its penetration inside the film signals the transition into the mixed phase, occurring when the field generated by the superconducting coil reaches H_{c1}, and resulting in a sudden increase of the surface resistance (Fig. 6). As the film thickness is much larger than the penetration depth, an accurate description of the penetration process must account for the effect of pinning which resists the penetration by generating a gradient in the distribution of penetrating fluxons [28]. In practice the value of H_p is therefore dependent on the value of the critical current in the film, in particular close to its interface with the substrate. Moreover macroscopic defects such as pinholes or cracks may affect the measurement and what is measured in practice is an effective penetration field, which may significantly differ from the lower critical field. However, the method provides a valuable relative information when comparing one cavity with another.

4. Data analysis: an example

According to Relation 3 the surface resistance R_s of a specific film can be written as the sum of three separate quantities which help the characterisation of its properties:

- the BCS resistance, R_{BCS}, a global property of the superconductor providing measurements of the average energy gap Δ and mean free path l [2, 3, 10],

- the residual resistance, R_{res}, a revelator of the presence of imperfections, such as impurities or defects, the effects of which are not accounted for by the mean free path l,

- the fluxon induced resistance, R_{fl}, a revelator of the presence of pinning centres, providing information about their pinning strength.

In the present section a specific type of film is used as an example to illustrate the method of data analysis. Depending on the way in which they were prepared, different films are observed to be characterised by different values of R_{BCS}, R_{res}, and R_{fl}. However, they share many qualitative features, and parameterisations having a same form for all films can be used to describe the dependence of R_{BCS}, R_{res}, and R_{fl} on different variables. As a result it is possible to reduce the quantitative differences observed between different films to a small set of variables.

The preparation of the specific type of film considered in the present section follows the standard procedure described in 3.2 (single cathode sputtering in an argon atmosphere). Only cavities yielding $R_{res} < 100$ nΩ are considered in the present analysis. In cases where there was indication of the presence of field emission, H_{rf} was kept below threshold. A total of 28 different films prepared according to the same standard method are included in the data sample.

4.1 The BCS resistance

Each set of measurements includes in general complete isothermal H_{rf} scans at $T \sim 4.2$ K, when the cryostat is vented to atmospheric pressure and at $T \sim 1.7$ K, when the BCS resistance has become negligible and where the low pumping speed on the cryostat bath causes its temperature to vary very slowly over the period of data collection. In-between these extreme temperatures, when the helium gas is being evacuated from the cryostat, smaller portions of the R_s vs H_{rf} plane have been explored. In the present data sample, R_{BCS} decreases from 400 nΩ to less than 1.7 nΩ when T decreases from 4.2 K to 1.7 K. As R_{res} usually obeys the inequality

$$R_{BCS}(1.7 \text{ K}) < R_{res} < R_{BCS}(4.2 \text{ K}),$$

the values of R_s measured at 1.7 and 4.2 K are in general good approximations to R_{res} and R_{BCS} (4.2 K) respectively. This feature implies that accurate and virtually uncorrelated measurements of R_{res} and R_{BCS} (4.2 K) are obtained from the data.

The dependence of R_{BCS} (4.2 K) on H_{rf} is shown in Fig. 7. Minor corrections, typically $< 2\%$, have been applied in order to refer the data to 4.20 K and 1.70 K precisely as the actual temperatures at which they were taken may have differed slightly from these reference values. The spread of the data of different films is small and has been included in the measurement errors when performing the average. As the residual resistances of different films display instead a large spread, this result supports the assumption of temperature independence of the residual resistance. The BCS resistance at 4.2 K is observed to increase with H_{rf} by 50% between 0 and $H_{rf}^{*} \sim 35$ mT. This feature is not specific to films and a similar increase is observed with bulk niobium (see Section 5.1). A parameterisation of the form R_{BCS} (4.2 K) $= R_{BCS}^{0}$ (1 + $\alpha_1 H_{rf} + \alpha_2 H_{rf}^{2}$) gives a good fit to the data. The limitation to first order of the perturbative expansion used in calculations available in the literature [2,3,10] prevents a precise comparison of the data with theory. The value of H_{rf}^{*} is about one sixth of the thermodynamic critical field.

In order to check the hypothesis that the H_{rf} and T dependence of R_{BCS} factorises, a few isothermal scans were performed at intermediate temperatures. Such a data set is shown in Fig. 8 where the validity of the factorisation is illustrated by the fact that different isothermal scans display a same relative H_{rf} dependence.

From its approximate expression (2), R_{BCS} is seen to depend both on the energy gap Δ (in the exponential) and the mean free path l (in the scale factor). Measuring R_{BCS} at a single temperature is not sufficient to disentangle the Δ and l dependence. Fig. 9 shows the temperature dependence of the ratio $r = R_{BCS}(T)/R_{BCS}(4.2\text{ K})$, numerator and denominator being measured at equal values of H_{rf}. According to Relation 2 this ratio is expected to be independent from the mean free path and to provide a direct measure of the energy gap,

$$\tilde{\Delta} = \frac{4.2\ T}{T - 4.2}\ ln\ \frac{r\ T}{4.2}. \tag{4}$$

This is illustrated in Fig. 10 where $\tilde{\Delta}$ is displayed for different values of the temperature and is indeed observed to take a constant value, $\tilde{\Delta} = 19.6 \pm 0.2$ K. This value is used in Fig. 9 to draw the line

$$r = \frac{4.2}{T}\ exp\left[-\tilde{\Delta}\left(\frac{1}{T} - \frac{1}{4.2}\right)\right]. \tag{5}$$

The above evaluation is only approximate, as is Relation 2 from which it has been derived. A more accurate comparison of the experimental results with theory implies a numerical calculation of the integrals entering the expression of the surface resistance in Ref. 2 and 3. For this purpose use is made of the computer code of Ref. 10 where the temperature dependence of the energy gap is parameterised in the form

$$\Delta(T) = \Delta(0)\ cos^{0.5}\left[\frac{\pi}{2}\left(\frac{T}{T_c}\right)^2\right] \tag{6}$$

where $\alpha = \Delta(0)/T_c$ is allowed to depart from its standard BCS value. In the range of parameters relevant to the present work the value of $\tilde{\alpha} = \tilde{\Delta}/T_c$ deduced from Relation 4 is observed to systematically deviate from the input value of $\alpha = \Delta(0)/T_c$ by 0.18 ± 0.05, a measure of the approximate nature of Relation 2. The result $\tilde{\Delta} = 19.6 \pm 0.2$ K obtained above, implies therefore $\alpha = \Delta(0)/T_c = 1.87 \pm 0.04$ for $T_c = 9.54 \pm 0.06$ K measured for standard films as described in 3.5. The measured value of α is in good agreement with results of other published measurements [29] and with theoretical expectation [12]. The deviation of the measured T_c value from its nominal value, 9.25 K, is the combined effect of the lattice distortion due to the different thermal expansion coefficients of the niobium film and copper substrate and of an intrinsic structural difference between film and bulk [30].

Fig. 11 illustrates the dependence on mean free path of the BCS resistance calculated [10] at $T = 4.2$ K for $T_c = 9.54$ K and $\alpha = 1.87$, using a London penetration depth $\lambda_L(0) = 27$ nm and a BCS coherence length $\xi_0 = 33$ nm (see below). The abscissa is $1 + 0.5\ \pi\ \xi_0/l$ which is measured from the temperature dependence of the resonance frequency near T_c as $\lambda_{rel}^2 = (\lambda(0)/\lambda_0)^2$, the experimental values being scaled by a factor 1.18 ± 0.10 accounting for a small (9%) possible error on the evaluation of the clean limit reference λ_0. Together with data of the present section ($R^0_{BCS} = 401 \pm 3$ nΩ , $\lambda_{rel} = 1.56 \pm 0.05$). Fig. 11 includes data measured on other types of niobium films and on bulk cavities (see following sections). They are scaled to $T_c = 9.54$ K by a normalisation factor $exp(-\alpha[9.54 - T_c]/4.2)$ in order to ease the comparison.

The values of $\lambda_L(0)$ and ξ_0 used in the calculation have been tuned to best fit the data, as illustrated in Fig. 12. They were evaluated by fixing the value of the ratio $\lambda_L(0)/\xi_0$ to 0.813 as obtained from the ratio $\kappa = 0.96\,\lambda_L(0)/\xi_0$ [13] and from the measurements of the Ginzburg-Landau parameter, $\kappa = 0.78$, performed by Auer and Ullmaier [31] and by Finnemore, Stromberg and Swenson [29] on very pure niobium samples. The resulting value, $\lambda_L(0) = 27 \pm 2$ nm, is consistent with but lower than values used in earlier publications [14] and obtained from the penetration depth data of Fig. 5, the combined value being $\lambda_L(0) = 29 \pm 3$ nm. The calculation reproduces well the main qualitative features of the data, in particular the existence of a minimum in a region of mean free path just below $l = \xi_0$. However the data scatter significantly around the calculated curve, limiting somewhat the quality of the fit.

4.2 The fluxon-induced resistance

When the flux trapping efficiency was measured, complete trapping was always observed in the films considered in the present section, $\varepsilon < 0.2\%$ to 99% confidence level. Moreover the trapped state was found to be relatively robust against external perturbations. It was unaffected by switching on and off the solenoid and by the presence of RF power in the cavity, and it did not significantly evolve over periods of several hours.

In a first step the fluxon-induced resistance, R_{fl}, is studied at 1.7 K where the contribution of the BCS resistance is negligible. For a given film, R_{fl} is obtained from the difference between data measured with and without trapped flux. Minor corrections are applied to the data in order to refer them to $T = 1.70$ K precisely and to ensure that both measurements correspond to identical values of H_{rf} in the subtraction procedure.

Fig. 13a displays the dependence of R_{fl} (1.7 K) on H_{rf} for all data measured with $H_{ext} = 3.52$ G. A linear form fits well the data. Above a cavity dependent threshold, R_{fl} (1.7 K) is often observed to increase faster with H_{rf}. As the study of this effect is not completed, the present analysis has been restricted to an H_{rf} range in which R_{fl} depends linearly on H_{rf}. Fig. 13b displays the dependence of R_{fl}(1.7 K) on H_{ext} for all data measured at $H_{rf} = 3.4 \pm 1.1$ mT. The fluxon-induced resistance is seen to be proportional to H_{ext}. Such a proportionality is expected when the losses induced by different fluxons are uncorrelated, *i.e.* when R_{fl} is simply the product of the number of trapped fluxons by the average surface resistance associated with the elementary loss induced by a single fluxon.

In both Figures 13a and 13b the spread of the measurements is small and included in the error bars. The qualitative features displayed in these figures are independent from the precise values of H_{ext} and H_{rf} chosen to draw them, suggesting a parameterisation of the form

$$R_{fl}(1.7\text{ K}) = (R_{fl}^0 + R_{fl}^1\,H_{rf})\,H_{ext}. \tag{7}$$

Its validity is illustrated in Fig. 14 and 15. Fig. 14 displays the dependence of R_{fl} (1.7 K) H_{ext} on H_{rf} and Fig. 15 the dependence of R_{fl}(1.7 K)$/(R_{fl}^0 + R_{fl}^1\,H_{rf})$ on H_{ext}. In both cases the small spread of the measurements is included in the error bars. A good fit to the data of Fig. 14 is obtained with $R_{fl}^0 = 4.8 \pm 0.1$ nΩ/G and $R_{fl}^1 = 1.13 \pm 0.05$ nΩ/G/mT. The strong H_{rf} dependence observed here (R_{fl} (1.7 K) doubles between 0 and 4.2 mT) contrasts with the weaker one observed for R_{BCS}. In the fluxon case the unpaired electrons are concentrated over small regions, in the 10^{-4} range of the cell area per Gauss of H_{ext} while in the R_{BCS} case they are distributed over the whole sample.

The proportionality of R_{fl} (1.7 K) to H_{ext} illustrated in Fig. 15, is not always obeyed. When R_{fl} exceeds a few hundred nΩ a steeper dependence on H_{ext} is sometimes observed. Moreover, films may occasionally display a threshold in H_{ext}, H_{thr}, below which R_{fl} (1.7 K) is observed to vanish. Such films are usually of bad quality, as evidenced by the large value of their residual resistance, and have been excluded from the present analysis. An extreme example of such a film is shown in Fig. 16. A possible explanation of this particular feature is the presence of a large density of small normal conducting defects (such as pin holes or cracks reaching down to the copper substrate) having dimensions in excess of the coherence length. Flux trapped in such defects does not induce any additional RF loss, as the defect was already normal conducting before trapping. The threshold in H_{ext} would then correspond to the saturation of such defects [32], above which R_{fl}(1.7 K) would increase in proportion to the number of additional trapped fluxons, *i.e.* to H_{ext} - H_{thr}. In the present data set allowance for the existence of a positive threshold improves slightly the fit of Fig. 15, yielding $H_{thr} = 0.3$ G on average. However small changes of the residual resistance have sometimes been observed between measurements performed at different values of H_{ext}, limiting the accuracy of this result.

The temperature dependence of the fluxon-induced resistance is illustrated in Fig. 17. The ratio of $R_{fl}(T)$ to $R_{fl}(1.7$ K$)$, where numerator and denominator are measured at identical values of H_{rf} and of H_{ext}, is displayed as a function of temperature. Between 1.7 K and 4.2 K it is observed to increase by a factor $k_{fl} = 2.72 \pm 0.01$.

4.3 The residual resistance

The 28 films considered in the present section were all prepared in the same way and could therefore be expected to have nearly identical values of R_{BCS}, R_{fl} and R_{res}. The results presented above have shown that such is indeed the case for R_{BCS} and R_{fl}. The residual resistances display instead large differences, implying the existence of variables that take different values for different films. One such variable is the roughness of the substrate, others may simply have escaped sufficient control during the manufacturing process.

In the present data sample the films having the lower values of the residual resistance had been grown on spun cavities. Their smaller grain size and lower roughness may indeed favour the formation of a more uniform film allowing for a broader span of acceptable angles of incidence in the sputtering process and offering a larger resistance to the mechanical and thermal stresses to which the resonator is exposed. A simple model of typical film defects, using sensible parameters, can simulate the measured values of R_{res} and of their dependence on H_{rf}. However, the *ad hoc* nature of such a model cannot exclude factors other than the macroscopic properties of the film and the quality of its adhesion to the substrate as being responsible for the observed residual resistances.

In several instances low values of the residual resistance have been maintained over a broad range of H_{rf} (Fig. 18). This result is in contradiction with the conjecture [33] that a steep H_{rf} dependence would be a feature inherent to the intrinsic nature of sputtered niobium films, as seems to be the case of some granular high T_c superconductors [34].

Finally it should be noted that in some cases slightly lower values of R_{res} are measured when scanning the H_{rf} range upwards rather than downwards, a hysteresis effect which can be understood in terms of small regions associated with higher thermal impedance at the film-substrate interface.

5. Results obtained with different types of films and with bulk resonators

The previous sections have illustrated how the measurements reported in the present work can be reduced to the following set of parameters:

- T_c, the critical temperature measured by observing the transition from the Meissner state at $H_{ext} << H_{c1}$,

- $\lambda_{rel} = 1 + 5\pi \, \xi_0/l)^{0.5}$, the zero temperature penetration depth, measured from the temperature dependence of the resonance frequency in the vicinity of T_c and normalized to its clean limit value,

- H_p, an effective penetration field measured at 1.7 K as the value of the external magnetic field at which the equatorial surface resistance starts increasing,

- RRR, the residual resistivity ratio measured on samples prepared in the same way as the resonator under study, or, destructively, on samples cut from that resonator,

- R^0_{BCS}, the BCS resistance at $T = 4.2$ K and $H_{rf} = 0$,

- H^*_{rf}, the value of the mean RF field where $R_{BCS} = 1.5 \, R^0_{BCS}$, a measure of the rate of increase of R_{BCS} with H_{rf},

- $\alpha = \Delta(0)/T_c$ (or equivalently its approximate value $\tilde{\alpha} = \tilde{\Delta}/T_c$ obtained from Relation 4), measured from the temperature dependence of the BCS resistance,

- R^0_{fl} and R^1_{fl}, describing the linear dependence of the fluxon-induced resistance R_{fl} on H_{ext} and H_{rf},

- $k_{fl} = R_{fl}(4.2\ \mathrm{K})/R_{fl}(1.7\ \mathrm{K})$, a measure of the temperature dependence of the fluxon-induced resistance.

As discussed in the previous section, many of these variables can be compared with published measurements available in the literature or with theoretical predictions. In addition to the variables in the above list, the trapping inefficiency ε and the residual resistance R_{res} are also measured. The former is only used to make sure that full flux trapping has been realised. The latter is measured as a function of H_{rf}. Understanding the factors that contribute to it is the ultimate goal of the study but is likely to imply a preliminary understanding of the factors contributing to R_{BCS} and R_{fl}. As a step in this direction the present section reviews measurements obtained with bulk resonators and with films prepared differently from the standard films considered in the previous section, by changing the nature of the noble gas used in the sputtering discharge or of the interface between the niobium film and the copper substrate. A summary of these measurements in terms of some of the parameters listed above is presented in Table 3.

5.1 Bulk niobium resonators

Five resonators have been studied, of which two, seamless, were made by lathe spinning [20], and three were made from pairs of deep-drawn half-cells subsequently electron-beam welded at the equator [23]. Apart from R^0_{fl} and R^1_{fl}, which are observed to differ significantly between the two types, the data display sufficient consistency to justify a description in terms of a single set of variables (as usual their spread is included in the error bars), giving evidence for very important differences between the responses to microwaves of film and bulk resonators.

While the measured value of α is consistent with that of standard films, the BCS resistance, $R^0_{BCS} = 905 \pm 12$ nΩ, is more than twice as large. This result is compared with theory in Fig. 11. The rate of increase of the BCS resistance as a function of H_{rf} is similar to that measured for standard films.

As for standard films, full trapping was observed when ε was measured but the measurement method prevents an accurate localisation of the pinning centres. In particular pinning may occur preferentially on the outer surface of the cavity wall and the fluxons may be free to move on the inner surface where the RF field penetrates. However, at variance with standard films, a large sensitivity to the presence of trapped fluxons is revealed. The measured values of R^0_{fl} are 342 ± 12 nΩ/G for deep-drawn cavities and 127 ± 4 nΩ/G for spun cavities, respectively 70 and 25 times larger than for standard films.

Some phenomena that were occasionally observed on film resonators never occurred with bulk resonators. They include a positive threshold in the H_{ext} dependence of R_{fl} a possible hysteretic dependence of R_{res} on H_{rf} an occasional kink in the H_{rf} dependence of R_{fl} and a possible deterioration of R_{res} with increasing H_{rf}. While the first two are indeed understood as film-specific phenomena, a clear understanding of the latter two is still lacking.

Four of the five resonators were heat-treated at 1000°C for 4 hours (see Section 3.1), one of them being subsequently re-treated at 1100°C, again for 4 hours. After heat treatment a removal by BCP of about 20 µm was sufficient to obtain a clean surface. The five data sets show similar results, including a small increase of the BCS resistance, consistent with the expected evolution of the *RRR* value. But the main new feature is a significant trapping inefficiency, with ε taking different values for different Hall probes, spanning the whole range between 0 and 1 and going hand in hand with a lack of reproducibility of the R_s measurements in successive trapping cycles. Unfortunately, an analysis of the nature of the fluxon movements when crossing the mixed phase would require much more powerful instrumentation than available in the present experiment. The small area covered by each of the Hall probes, comparable to that of a grain in the heat-treated case, and the bad geometry (the probes being on the outer side of the 3mm thick niobium wall while the RF field penetrates from the inner side) prevent a reliable interpretation of the data. As a consequence it is only possible to quote approximate values of R^0_{fl} and R^1_{fl}. While R^0_{fl} exceeds 200 nΩ/G, R^1_{fl} has now become smaller than 1 nΩ/G/mT and may even have vanished.

5.2 Noble gas contamination

Films are observed to be contaminated by atoms of the noble gas used in maintaining the sputtering discharge. The noble gas concentration in the film depends on the discharge parameters, on the coating temperature and on the atomic mass of the noble gas [35]. The heavier the noble gas ions, the less likely it is for them to bounce back into the film after having been projected towards the niobium cathode and neutralised. Changing the nature of the noble gas provides a simple way to change its concentration in the film (see Table 2). In the present subsection results obtained with neon, krypton and xenon are presented and compared with the standard argon data. However, neon discharges result in a very high contamination of the film, to such an extent that its superconducting properties severely deteriorate. In order to keep the explored range of gas concentrations within reasonable limits, neon-argon mixtures have been used in various proportions. It has been found that a 50% Ne, 50% Ar composition of the discharge gas results in a gas concentration in the film approximately 50 times as large as for standard argon films.

The measured relative values of the penetration depth at $T = 0$, λ_{rel}, and of the effective penetration field at $T = 1.7$ K, H_{rel}, normalised to their values in the bulk heat-treated case taken as a clean limit reference, are observed to be correlated. The dependence of H_{rel}^{-2} on λ_{rel}^{2} is illustrated in Fig. 19. Fig. 20 compares the values of ξ_0/l deduced from the penetration depth measurements, with independent evaluations deduced from RRR measurements of sample films prepared under similar conditions as the cavities. The data are from films grown in argon-neon mixtures of various proportions. The reasonable agreement between the two sets gives confidence in the overall procedure. The critical temperature and the energy gap (Table 3) are observed to be relatively insensitive to the presence of noble gas impurities up to concentrations of the order of 2 to 3 atomic percent, higher than measured for other gases such as oxygen [36].

The dependence on mean free path of the BCS resistance at 4.2 K is illustrated in Fig. 11 and has been discussed in Section 4.1. The dependence on mean free path of the fluxon-induced losses is illustrated in Fig. 21, which displays the variations of R^0_{fl} and R^1_{fl} with λ_{rel}^{2}. In both cases a steep rise is observed towards large values of λ_{rel}^{2}, namely low values of the mean free path. The krypton data have particularly low R_{fl} values, lower than that of the Xe, Ar and Ar/Ne data at similar values of the mean free path. This feature is clearly visible in Fig. 22 where the data are displayed in the R^1_{fl} vs R^0_{fl} plane, taking advantage of the better accuracy of the R_{fl} measurements (as compared to λ_{rel} measurements) and making use of the whole data sample (λ_{rel} was not measured in the early phase of the experiment).

Fig. 23 displays the dependence of k_{fl} on λ_{rel}^{2}. The temperature dependence of the fluxon-induced losses is observed to be only weakly dependent on mean free path. It is maximal in the region $l \approx \xi_0$ where both R_{fl} and R^0_{BCS} are minimal.

The influence on residual resistance of the noble gas concentration is difficult to evaluate, large spreads being observed between films grown following the same procedure. For mean free paths in excess of approximately 20 nm, very low residual resistances are occasionally measured, suggesting that noble gas concentrations lower than approximately 0.5 atomic percent do not cause any significant deterioration of the residual resistance. However, important deterioration, both of the $H_{rf} = 0$ value and of the rate of increase with H_{rf} is observed for noble gas concentrations larger than about 3 atomic percent.

5.3 The film substrate interface

The double-cathode sputtering system described in 3.2 was used to produce films free of an intermediate oxide layer at the copper-niobium interface. The results are listed in Table 3 and displayed in Figures 11, 18 and 21 to 23. They differ from the data studied in the preceding subsection in many respects. In particular they have lower values of the critical temperature and of the penetration depth.

Fig. 24 displays the dependence of the coupling parameter on critical temperature for standard films (having an oxide interface) and for oxide free films (obtained by reverse sputtering). Also shown are measurements made on films grown on the copper substrate after having baked it out at ~ 300°C in UHV for at least 20 hours and on films grown on the double cathode system vented to air after the reverse sputtering operation. While the coupling parameters take mutually consistent values in each set of data, the critical temperatures display significant differences. Films grown on oxide free copper have a lower critical

temperature than films grown on oxidised copper. The intermediate values obtained for the other two sets are consistent with this observation: copper substrates should become nearly oxide free after having been baked out and should become oxidised after having been vented to air. Films grown on a 1.5 μm thick under-layer sputter-coated on the oxidised copper substrate, but itself prevented from getting oxidised, confirm the observed trend. On a titanium under-layer they have the same critical temperature as standard films and the same values of all other variables, while on a copper under-layer they have the same critical temperature as oxide free films and the same values of all other variables. It might be argued that the difference in critical temperature could be restricted to a region near the interface between the film and the substrate (T_c is measured by letting magnetic field penetrate in the film from the side of the interface). However, as it was usually possible to observe on a spectrum analyser the loss of the frequency lock and to record the associated temperature, the consistency of the superficial and interfacial values of the critical temperature could be checked to within ~ 0.05 K.

It seems that the nature of the substrate on which the film is grown is determinant in defining its properties. The same observation is made when comparing the penetration depths, oxide free films behaving more like bulk niobium than standard films do. For a same composition of the discharge gas the suppression of the oxide layer at the interface results in a decrease by nearly one unit of ξ_0/l. This result has been confirmed by RRR measurements.

The variables describing the properties of the surface resistance, such as R_{fl} and $R^0_{BCS,}$ take values consistent with the trends observed in the preceding subsections (see Fig. 21 to 23). The "clean" region explored by the oxide free data shows the expected evolution towards the clean limit reference of heat-treated bulk data. Moreover oxide-free films are observed to yield significantly lower values of the effective penetration field H_{rel} than standard films do for a same value of λ_{rel} (Fig. 18). This may be the result of a weaker pinning causing a smaller gradient of the density of penetrating fluxons and a lesser resistance to their penetration.

Finally the measured residual resistances are again observed to vary from cavity to cavity in an apparently uncontrolled manner. On average, however, oxide-free films display larger values both of the mean residual resistance and of its rate of increase with H_{rf}. Moreover, other differences have been observed between the two kinds of films. Films grown on oxide free copper have a lower value of H_{thr} (on the average 0.1 G) than films grown on oxidised copper (on the average 0.3 G). The latter display often a sudden increase of R^l_{fl} at a cavity dependent value of H_{rf}, the former never do. And the width of the ΔH_{eff} transition at $T = T_c$ (see Section 3.5) is narrower in the oxidised case than in the oxide free case.

6. Discussion of the results

6.1 General comments

In spite of the large area of the resonator walls, ~ 670 cm^2, perfectly reproducible data have been obtained, allowing for the detection of rather subtle effects, with however one exception, the residual resistance. All other variables, including the critical temperature, the penetration depth, the gap, the BCS resistance, the fluxon-induced resistance and the penetration field, were found consistent within errors when measured on different resonators prepared under identical conditions. Evidence for this is not new and was implicit in several

earlier publications [14]. As a result, differences observed between resonators prepared under different conditions could be relied upon and could provide valuable information on the underlying physics, as further developed later in this section.

Such is not the case of the residual resistance, which was observed to vary between typically 1 and 50 nΩ in an uncontrolled way. This situation did not obscure the understanding of the other parameters, a result of the absence of correlation between these and the residual resistance. It would have, of course, if the quantity and the quality of the measurements made had not allowed for an accurate subtraction of the effects of the residual resistance. In practical applications, such as the production of accelerating cavities, it is essential to control the residual resistance and to keep its value below, say, 10 nΩ over a very broad range of RF field amplitude. As this is an important topic, we return to it at the end of this section.

6.2 The BCS resistance

An important result of the present study is the observation of regularities displayed by the BCS resistance and by the fluxon-induced resistance as a function of mean free path l. Different components of the surface resistance have different sensitivities to l. The BCS surface resistance, for which a theoretical prediction is available with essentially no free parameter, is minimal in the region below $l = \xi_0$ and typically doubles at the edges of the explored l range. The fluxon-induced resistance, which is also minimal near $l = \xi_0$, increases by a factor ~ 50 over the same range.

The general agreement between the measured and theoretical values of the BCS resistance (Fig. 11), and in particular the observation of the predicted minimum below $l = \xi_0$, give confidence in the understanding of the underlying physics. In the theory, the existence of a minimum is the result of the resonant behaviour of photon absorption by thermally excited quasiparticles [10]. In the clean limit, photon absorption is dominated by photon momenta transferred between quasiparticle states having a kinetic energy difference matching optimally their density of states. As l decreases and gets closer to ξ_0 the peak of momentum transfer efficiency broadens significantly and the penetration depth increases slowly, the net result being a decrease of the BCS resistance. When l decreases below ξ_0 the penetration depth starts increasing faster and overtakes the resonance broadening effect, causing the increase of the BCS resistance. It is remarkable that such a subtle effect could be experimentally observed. Quantitatively, however, the agreement is of limited quality. The reason is a significant spread of the data points around the predicted curve. The spread is not the result of a lack of control of the measurement errors, films produced under exactly the same conditions giving consistent R^0_{BCS} values, but it is the effect both of the large relative uncertainties on λ_{rel}^2 and of small R^0_{BCS} differences associated with the detailed conditions under which the film was grown. In other words, the mean free path is sufficient to describe the gross features of the data but not to account for the finer details.

Another result of the present data, which had not been explicitly stated in earlier publications, is the observation of an increase of the BCS resistance (measured at 4.2 K) with the amplitude of the RF field by 50% between 0 and 32 ± 5 mT, independently from the value of the mean free path.

6.3 Fluxon-induced losses

Before commenting on the results related to fluxon-induced losses it is useful to recall the geometry and to evaluate a few relevant parameters. As shown in Fig. 25, at any point of the cavity inner surface the RF magnetic field component H_{rf} is tangent to the parallel circle P of the point and the induced current $J \propto H_{rf}$ is tangent to the meridian M of the point. The external field is parallel to the cavity axis, implying that the fluxons are nearly parallel to the film at the equator and nearly normal to it farther away. While there is no reason to doubt that the field nucleates when the resonator is cooled down across critical temperature, there is no direct evidence that it does it in the form of a uniform triangular fluxon lattice. In fact there is ample evidence for the occasional occurrence of a non uniform nucleation in the case of type II superconductors having a low value of the Ginzburg-Landau parameter [9]. In any case, if a fluxon Φ_0 is trapped parallel to the external field, the Lorentz force $J \times \Phi_0/c$ acting on it will always be tangent to P but will vanish both at the equator (where J and Φ_0 are parallel) and at the iris (where H_{rf} itself vanishes). It is unlikely that the trapped equatorial fluxons be exactly parallel to the external field and, even if they are, instabilities are known to occur in this parallel geometry [9]. It is nevertheless useful to calculate the geometrical sensitivity to fluxon induced losses,

$$\sigma_g = <H_{rf}\, sin\ \theta_m > / <H_{rf}>,$$

where the averages are taken over the cavity surface and where θ_m is the angle between the meridian and the cavity axis (Fig. 25). The result, $\sigma_g = 0.59$, is an approximate measure of the factor by which R_{fl} is reduced with respect to an ideal geometry where H_{ext} would be normal to the film surface everywhere.

The viscosity parameter that governs the flow of unpinned fluxons is, in the approximation of the Bardeen-Stephen model [16],

$$\eta = H_{c2}\, \Phi_0 / (\rho_n\, c^2) \qquad (8)$$

where ρ_n is the normal state resistivity, H_{c2} the upper critical field and $\Phi_0 = hc/2e$. A constant uniform current density J sets the unpinned fluxon lattice in motion at constant velocity v_{fl} such that

$$\eta\, v_{fl} = J\Phi_0\ sin\ \theta_m / c. \qquad (9)$$

In the present study the current density is neither constant nor uniform but v_{fl} provides a useful reference scale. An upper limit to the amplitude of the fluxon oscillations is

$$y_{fl} = v_{fl} / 2\pi f\ = J\ \Phi_0\ \sigma_g\ / (2\pi f\, \eta\, c). \qquad (10)$$

Models [16] such as that of Gittleman and Rosenblum (GR) and that of Clem and Coffey (CC) extend the Bardeen-Stephen model to the microwave region. While CC include numerous sophistications (non-locality, flux creep and thermal activation) these are not essential to the present data. In the GR model the dissipation vanishes if the fluxons do not move but as soon as they move the surface resistance is essentially measured by its normal state value, R_n, scaled down by a factor H_{ext}/H_{c2}. In the CC model excitations of the quasi particles in the fluxon cores are taken in proper account and dissipation occurs even for non-moving fluxons, again essentially governed by $R_n\, H_{ext} / H_{c2}$. The quantity R_n/H_{c2} is therefore a useful reference with which to compare the measured values of R^0_{fl}.

In the clean case (RRR=300), ρ_n=0.05 $\mu\Omega$cm, R_n=1.7 mΩ and H_{c2} decreases from 4.2 kG at T=0 to 4.0 kG at T=1.7K and 2.7 kG at T=4.2K [29]. When inserting these values in Relations (8) and (10) one obtains $y_{fl}/H_{rf} \cong 3$ nm/mT, giving the scale of the amplitude of the fluxon oscillations. The scale of R_{fl} is given by

$$\sigma_g R_n / H_{c2}(1.7K)=250 \text{ n}\Omega/\text{G},$$

of the same order of magnitude as the values of R_{fl}^0 measured on heat-treated bulk cavities. As l decreases one expects R_n/H_{c2} to vary smoothly, in clear disagreement with the experimental observation of a sharp R_{fl} minimum near $l=\xi_0$. The measured value of R_{fl} in the region of the minimum is also much too low to be caused by sensible variations of R_n and H_{c2}. Near $l=\xi_0$, $RRR = 15$, $R_n = 8$ mΩ and $R_{fl}^0 = 4$ nΩ/G, which would imply $H_{c2}(1.7K) = 1150$ kG. There exists an abundant literature [37] on the dependence of H_{c2} on temperature and mean free path in niobium. Using the data of Koch, Scarbrough and Kroeger [37] one estimates $H_{c2}(1.7K) = 6$ kG for $RRR = 15$, instead of 1150 kG obtained above. The mismatch between the two numbers is much too large, it nearly reaches a factor of 200. One might argue that the value of H_{c2} might be much higher for film than for bulk at equal values of RRR. The value of H_{c2} can in principle be deduced from magnetisation measurements or from inductive measurements [28, 37]. However, as abundantly documented in the literature, several factors make the interpretation of such data particularly difficult. They include the existence of a very strong surface pinning, that of a surface superconductivity extending to $H_{c3} = 1.7 H_{c2}$ and, more generally, an extreme sensitivity to the presence of oxygen and to the nature of the surface treatment [37]. Measurements on films are scarce [38] and may suffer in addition from the presence of eddy currents in the copper substrate. Two samples coated with standard niobium films were measured inductively at Wuppertal University after dissolution of the copper substrate in a nitric acid solution [39]. The result, 4.5 kG $< H_{c2}(4.2$ K$) <$8.5 kG, is to be compared with the value $H_{c2}(4.2K) = 5$ kG estimated from the data of Koch, Scarbrough and Kroeger [37]. This confirms that there is no reason to invoke an anomalous behaviour of H_{c2} to explain the deep minimum displayed by R_{fl} near $l = \xi_0$. Its understanding remains a challenge of the present data.

Both the BCS resistance and the fluxon-induced resistance are minimal in the region of $l \sim \xi_0$. As the only available length scale in the low T range of the present study is $\lambda_L(0) \sim \xi_0 \sim 30$ nm, such a coincidence may be less surprising than it seems at first sight. It is nevertheless natural to explore the possibility that a same cause be at the origin of the minima of R_{BCS} and R_{fl}. However, such an hypothesis does not seem easily tenable because of the very different shallowness of the two minima. Moreover, it is difficult to see how the physics origin of the R_{BCS} minimum, which we believe to understand, might relate to R_{fl}.

Pinning remains therefore the most likely candidate as the mechanism responsible for the suppression of R_{fl} below the clean limit value when l is in the vicinity of ξ_0. Pinning may result from the presence of impurities, of defects or simply from the roughness of the film surface, including the interface with the substrate. In the configuration of the presentexperiment, with $H_{ext} << H_{c1}$, the density of the lattice, and therefore its rigidity, are low. As the most efficient pinning is expected from dense but not overlapping pinning centres [40] one could imagine that such is the case for $l \sim \xi_0$. However, films grown in a krypton discharge, for which R_{fl} is minimal, contain approximately 10 atomic ppm of krypton, namely ~ 1000 atoms in a 1.5 μm long fluxon core traversing the film across its thickness, much too

large a number to make the hypothesis tenable. For pinning to be responsible for the observed R_{fl} minimum it would take a much smaller concentration of pinning centres. This could be achieved in practice if the krypton atoms were not uniformly distributed in the film but would instead cluster, as can in fact be expected to be the case. Indeed, ion-implanted noble gases are known to precipitate in the form of solid, overpressurized crystals containing typically a few thousand atoms [41], namely of the right size to account for the effect. Such considerations may help the understanding of the pinning mechanism and of the fluxon-induced RF losses. However they do not seem sufficient to justify such a steep and narrow R_{fl} minimum. Similar considerations have been made by Ji, Rzchowski and Tinkham [42] in the context of polycrystalline high T_c cuprates.

The large values taken by R_{fl}^1 cannot be ignored when seeking an interpretation of the present data, it dominates the fluxon-induced losses over most of the explored H_{rf} range. In a picture where pinning is the relevant mechanism it could imply that a lesser fraction of the fluxons' length stays pinned as H_{rf} increases, or that depinning occurs progressively, at lower values of H_{rf} for the less strongly pinned fluxons and at higher values of H_{rf} for the more strongly pinned fluxons.

It is interesting to remark that $\sigma_g R_n/H_{c2}$ increases by a factor 1.5 when T increases from 1.7 K to 4.2 K, matching exactly the value of k_{fl} measured on bulk niobium cavities. However, it is not clear why k_{fl} should depend on mean free path and double in the region where R_{fl} is minimal.

Finally it must be noted that, as in the case of R_{BCS}, the mean free path is sufficient to describe the gross features of the data but not to account for finer details, such as the very low R_{fl} values obtained with krypton in the region $l \sim \xi_0$.

6.4 The film substrate interface

A particularly interesting and unexpected result of the present work is the observation of a significant sensitivity of the film properties to the nature of its interface with the substrate. In particular, for xenon, krypton and argon discharges the critical temperature is nearly 0.2 K lower and the ratio ξ_0 / l nearly one unit lower for films grown on oxide free copper than for films grown on oxidised copper or on a titanium under-layer.

Additional information on the difference between the two kinds of films has been obtained from the analysis of samples cut from two cavities, one of each kind. The measured RRR values, 11.5 ± 0.5 and 29 ± 1 respectively, confirm the expected difference. More surprising are the X-ray diffraction spectra, which reveal major differences between the textures of the two films. Fig. 26 displays the Bragg spectra measured on each of the two samples with a monochromatic incident beam (K_α of copper). As both films are ~ 1.5 μm thick and the X-ray attenuation length in niobium is ~ 7.5 μm, the copper substrate (fcc) is visible. In the oxidised case, the film (bcc) grows quasi exclusively with the (110) plane (the most densely packed plane) parallel to the copper surface. In the oxide free case, on the contrary, the (211) and (200) planes are equally probable. Room temperature values of the lattice parameters are deduced from the spectra and found to be only slightly different, 0.3318 ± 0.0002 nm in the oxide free case and 0.3324 ± 0.0002 nm in the oxidised case. As already suggested from the difference observed between the critical temperatures, this implies larger stresses in films grown on oxidised copper than in films grown on oxide free copper. Also, the argon concentration, measured by thermal extraction, is smaller in the oxide free case,

explaining at least part of the observed difference between the corresponding mean free paths. Further study is necessary in order to better understand what relates the observed differences between the two kinds of films, namely the differences observed between their textures, stresses and argon concentrations.

6.5 Residual resistances

An important result of the present work is the evidence against any significant correlation between the residual resistances (as long as they do not exceed a few 100 nΩ and the other measured variables (T_c, Δ, R_{BCS}, R_{fl}, λ_{rel} and H_{rel}). What is meant here is that films prepared under exactly the same conditions yield mutually consistent values of these other variables, but often inconsistent values of the residual resistances. Moreover large differences between the measured residual resistances do not affect the consistency of the other variables. This does not mean that the range covered by the measured residual resistances is always the same, independently from the mode of preparation of the film. In fact we observe that, on average, films grown on oxide free copper display a larger residual resistance than films grown on oxidised copper. Each residual resistance can often be characterised by two variables, R^0_{res} and $R^1_{res,}$ adjusted to fit the form

$$R_{res} = R^0_{res} + R^1_{res} H_{rf}$$

over the range in which it gives a reasonable description of the data, in particular below the H_{rf} value where R_{res} starts increasing abruptly and is often accompanied by field emission. The variables R^0_{res} and R^1_{res} are observed to be positively correlated.

The absence of correlation between the residual resistance and the other variables suggests that whatever is causing R_{res} to deviate from zero is not associated with intragranular variables but rather with extragranular non-superconducting regions. Other than sporadic macroscopic defects, a trivial source of residual resistance, grain boundaries are obvious candidates and several authors [33, 34] have studied their effect under the assumption that they behave as dissipative junctions connecting superconducting grains. While such junctions would contribute to the power dissipation of quasiparticles, and therefore to the BCS resistance, they are also expected to contribute to the temperature independent power dissipation of supercurrents in the Josephson regime, and therefore to the residual resistance. Attanasio *et al.* [33], analysing 500 MHz data under the assumption that this is the dominant dissipation mechanism, find a residual resistance of 57 nΩ for standard films at low values of H_{rf}. Using the same film parameters at 1.5 GHz would imply a residual resistance exceeding 500 nΩ, which is clearly too large when compared to the results of the present study. Also the overall low temperature dc resistivity of their model film is 6 $\mu\Omega$cm instead of 1.4 $\mu\Omega$cm in the present data. It is difficult to find a sensible set of film parameters which could describe the observed spread of standard film residual resistances, typically ranging between 1 and 50 nΩ for R^0_{res} and between 0.2 and 5 nΩ/mT for R^1_{res}. The approach of Bonin and Safa [33], who were aware of this difficulty, is to postulate the existence of a low critical current tail in the distribution of the junctions' critical currents. The effect is then blamed exclusively on junctions working near or above their critical current and the shape of the tail is adjusted *ad hoc* to reproduce the dependence of R_{res} on H_{rf} with the correct value of R^1_{res}. While it is not unreasonable to suspect important fluctuations in the tail of the critical current distribution of supposedly identical cavities, this approach has the disadvantage of requiring different mechanisms to describe R^0_{res} and R^1_{res}, when the data show a clear correlation between the two variables. In summary, while the data suggest that the residual resistances are indeed the

result of extragranular dissipation, they do not support the junction models developed in Ref. [33]. The large spread of the data makes it difficult to find an even qualitatively acceptable description of the present results in terms of such models.

In the bulk niobium case a well-known and abundantly documented cause of RF losses [43, 44] is the possible precipitation of hydride when the hydrogen concentration is large enough and the concentration of other impurities small enough. The niobium-hydrogen phase diagram has been studied in detail over a broad range of temperature and concentration [43]. The niobium-hydrogen system is characterised by a very large diffusion constant, a high solubility and a rather complex phase diagram. The possible occurrence of hydride precipitation depends on the detailed conditions under which the phase diagram is traversed when going from room temperature to liquid helium temperature, the kinetics of the relevant transformations playing an essential role. Another determinant factor is the concentration of other impurities, such as oxygen, which may serve as trapping centres for hydrogen. While hydride precipitation is an important and well established source of residual resistance [44] the exact conditions which govern its occurrence are not fully understood and its prevention is not completely mastered. In order to study its possible contribution to the residual resistance of films, we have loaded a few film cavities with hydrogen in concentrations ranging between 0.5 and 2.5 atomic percent. Residual resistances as large as a few $\mu\Omega$ and displaying a correlation between R^0_{res} and R^1_{res} similar to that observed in the normal data have been obtained this way with virtually no incidence on the other variables. The effect seems to be enhanced for films grown on oxide free copper in comparison with films grown on oxidised copper.

Moreover, films grown on an oxide free copper substrate are often seen to have a residual resistance that increases with the temperature gradient present in the cavity region during cool-down across T_c. Such thermoelectric effects have been observed earlier [45] with niobium-tin films. In most cases, however, they are not an important source of residual resistance and, when they are, the temperature gradient can easily be kept below dangerous level.

6.6 Conclusions

The present study has made available an important set of new measurements of the RF properties of superconducting niobium films, which usefully complement earlier published data [46]. Many new results have been obtained on the detailed behaviour of the surface resistance, in particular its BCS and fluxon-induced terms, and on the properties of niobium films. New methods of analysis have been devised that may be of interest to a broader class of experiments. A number of misconceptions commonly held about the RF properties of niobium films, including in particular blaming the strong R_{fl} minimum on an anomalous H_{c2} behaviour and postulating the existence of major unavoidable limitations on their residual resistance (in particular its H_{rf} dependence), have been corrected. However, while we know of no major fundamental limitation to the film approach, more work is necessary in order to identify better the factors contributing to the residual resistance and, hopefully, to devise appropriate cures.

Acknowledgements

References

[1]   J. Bardeen, L.N. Cooper and J.R. Schrieffer, Phys. Rev. 108 (1957) 1175.

[2]   D.C. Mattis and J. Bardeen, Phys. Rev. 111 (1958) 412.

[3]   A.A. Abrikosov, L.P. Gor'kov and I.M. Khalatnikov, Zh. Eks. Teor. Fiz 35 (1958) 265 and JETP 35 (1959) 182.

[4]   H. Padamsee, K.W. Shepard and R. Sundelin, Ann. Rev. Nucl. Part. Sci. 43 (1993) 635.

[5]   D. Boussard, Proc. of the 5th European Part. Conf., EPAC '96, (S. Myers et al. ed. Barcelona, Spain 1996), page 187.

[6]   C. Benvenuti, N. Circelli and M. Hauer, Appl. Phys. Lett. 45 (1984) 583,

C. Benvenuti, Part. Accel. 40 (1992) 43,

G. Cavallari, C. Arnaud, M. Barranco-Luque, C. Benvenuti, Ph. Bernard, D. Bloess, D. Boussard, P. Brown, S. Calatroni, E. Chiaveri, E. Ciapala, G. Gesconke, D. Güsewell, E. Haebel, N. Hilleret, G. Orlandi, G. Passardi, E. Peschardt, V. Roedel, T. Schiller, M. Taufer, J. Tueckmantel, J. Uythoven and W. Weingarten, Proc. of the 6th Workshop on RF Superconductivity, (R. Sundelin ed., CEBAF, Newport News, USA 1993), 1, page 49.

[7]   H.A. Grunder, Proc. of the 16th Particle Accelerator Conference - PAC 95 (Dallas, USA, 1995), 1, page 1.

[8]   R. Brinkmann, Proc of the 16th Particle Accelerator Conference - PAC 95 (Dallas, USA, 1995), 1, page 674,

D. Proch, Proc. of the 6th Workshop on RF Superconductivity, (R. Sundelin ed., CEBAF, Newport News, USA 1993), 1, page 382.

[9]   A.A. Abrikosov, Zh. Eks. Teor. Fiz. 32 (1957) 1442 and JETP 5 (1957) 1174,

A.M. Campell and J.E. Evetts, Adv. in Phys. 21 (1972) 199 and references therein.

[10] J. Halbritter, Z. Phys. 266 (1974) 209 and Externer Bericht 3/70-6, Kernforschungzentrum Karlsruhe, Germany, June 1970.

[11] G.M. Eliashberg, Zh. Eks. Teor. Fiz. 38 (1960) 966 and JETP 11 (1960) 696,

P.B. Miller, Phys. Rev. 113 (1958) 1209 and Phys. Rev. 118 (1960) 928,

G. Rickaysen, Phys. Rev. 115 (1959) 795,

T. Tsuneto, Phys. Rev. 118 (1960) 1029,

D.J. Scalapino, J.R. Schrieffer and J.W. Wilkins, Phys. Rev. 148 (1966) 263,

S.B. Nam, Phys. Rev. 156 (1966) 470 and 487,

R. Blaschke, J. Ashkenazi, O. Pictet, D.D. Koelling, A.T. van Kessel and F.M. Mueller, J. Phys. F: Met. Phys. 14 (1984) 175,

R. Poepel, J. Appl. Phys. 66 (1989) 595,

R. Blaschke and R. Blocksdorf, Z. Phys. B49 (1982) 99.

[12] J.P. Carbotte, Rev.Mod. Phys. 62 (1990) 1027 and references therein.

[13] L.P. Gor'kov, Zh. Eks. Teor. Fiz. 36 (1959) 1918 and JETP 36 (1959) 1364,

V.L. Ginzburg, Zh. Eksp. Teor. Fiz, 34 (1958) 113,

J. Matricon and D.St. James, Phys. Lett. 24A (1967) 241,

T. Yogi, G. J. Dick and J. E. Mercereau, Phys. Rev. Lett. 39 (1977) 826.

[14] J.P. Turneaure, J. Halbritter and H.A. Schwettman, J. Supercond. 4 (1991) 341,

H. Padamsee, J. Knobloch and T. Hays, RF superconductivity for accelerators, John Wiley and sons inc., New York, 1998.

[15] F.L. Palmer, Ph. D. Dissertation, Cornell University, Ithaca N.Y., USA, 1988 and references therein,

J. Halbritter, Proc. of the 2nd Workshop on RF superconductivity, (H. Lengeler ed., CERN, Geneva, 1984), page 427.

[16] J. Bardeen and M.J. Stephen, Phys. Rev. A140 (1965) 1197,

L.P. Gor'kov and N.B. Kopnin Usp. Fiz. Nauk. 116 (1975) 413 and Sov. Phys. Usp. 18 (1976) 496 and references therein,

J.I. Gittleman and B. Rosenblum, J. Appl. Phys. 39 (1968) 2617,

M. Rabinowitz, Lett. Nuovo Cimento 4 (1970) 549,

J.R. Clem and M.W. Coffey, J. Supercond. 5 (1992) 313,

A.E. Koshelev and V.M. Vinokur, Physica C 173 (1991) 465,

T.C. Hsu, Physica C 213 (1993) 305,

G. Blatter, M.V. Feigel'man, V.B. Geshkenbein, A.I. Larkin and V.M. Vinokur, Rev. Mod. Phys. 66 (1994) 1125 and references therein,

E.H. Brandt, Rep. Prog. Phys. 58 (1995) 1465 and references therein.

[17] P. Kneisel, R. Vincon and J. Halbritter, Nucl. Inst. Meth. 188 (1981) 669,

V. Lagomarsino, G. Manuzio, R. Parodi and R. Vaccarone, IEEE Trans. Mag. 15 (1) (1979) 25.

[18] D. Moffat, P. Barnes, T. Flynn, J. Graber, L. Hand, W. Hartung, T. Hays, J. Kirchgessner, J. Knobloch, R. Noer, H. Padamsee, D. Rubin and J. Sears, Part. Accel. 40 (1992) 85 and references therein.

[19] C. Hauviller, Proc. of the 14th IEEE Particle Accelerator Conference - PAC 89 (F. Bennett and J. Kopta eds., Chigago, USA 1989), 1, page 485.

[20] V. Palmieri, Part. Accel. 53 (1996) 217.

[21] "Theory and Practice of Pulse Plating" ed. J.C. Puippe, F.Leaman, AESF, Orlando, Fl., USA, 1986,

M. Viswanathan, Proc. of the International Conference on Electrodeposition and Electroforming, (E.S. Dwarakadasa, R.P. Dampal and J. Balachandra eds., Indian Institute of Science, Bangalore, India 1986), page 177,

S. Parussatti, Note Technique MT-SM/94-10, CERN, Switzerland, 1994, unpublished.

[22] J.P. Birabeau and J.M.A. Guerin, Patent N° 88 09820, Institut National de la Propriété Industrielle, 1993.

[23] P. Kneisel, J. Mammosser, G. Rao, K. Saito and R. Sunderlin, Conf. Record of the 15th IEEE Particle Accelerator Conference – PAC 91 (San Francisco, USA, 1991), 4, page 2384.

[24] C. Benvenuti, S. Calatroni, M. Hauer, G.Orlandi and F. Scalambrin, Proc. of the 6th Workshop on RF Superconductivity, (R. Sundelin ed., CEBAF, Newport News, USA 1993), 2, page 676.

[25] J. Halbritter, Appl. Phys. A43 (1987) 1 and references therein,

I. Lindau and W.E. Spicer, J. Appl. Phys. 45 (1974) 3720.

[26] H. Ljungcrantz et al., J. Vac. Sci. Technol. A 11(3) (1993) 543,

R. Kuzel, Jr., R.Cherny, V. Valvoda, M. Blomberg and M. Merisolo, Thin Solid Films, 247 (1994) 64,

D.W. Hoffman, J. Vac. Sci. Technol. A12-4 (1994) 953.

[27] J. Halbritter, Z. Phys. 243 (1971) 201.

[28] C.P. Bean, Rev. Mod. Phys. 36 (1964) 31,
      A.M. Campbell, J. Phys. C4 (1971) 3186 and references therein.

[29] D.K. Finnemore, T.F. Stromberg and C.A. Swenson, Phys. Rev. 149 (1966) 231,
      H.A. Leupold and H.A. Boorse, Phys. Rev. 134 (1965) A1322,
      E.R. Dobbs and J.M. Perez, Rev. Mod. Phys. 36 (1964) 257,
      Levy, R. Kagiwada and I. Rudwick, Phys. Rev. 132 (1963) 2039,
      L. Giaever, 8th Int. Conf. on Low Temp. Phys. 1962, unpublished,
      M.D. Sherril and H.H. Edwards, Phys. Rev. Lett. 6 (1961) 460,
      P. Townsend and J. Sutton, Phys. Rev. 128 (1962) 591,
      M.A. Golosovsky, H.J. Snortland and M.R. Beasley, Phys. Rev. B51 (1995) 6462,
      A. Philipp and J. Halbritter, IEEE Trans. Mag., MAG-17 (1981) 951 and 19 (1983) 999,
      J.P. Turneaure and I. Weissman, J. Appl. Phys. 39 (1968) 4417.

[30] G. Heim and E. Kay, J. Appl. Phys. 46 (1975) 4006 and references therein.

[31] J. Auer and H. Ullmaier, Phys. Rev. B7 (1973) 136,
      B.W. Maxfield and W.L. McLean, Phys. Rev. 134 (1965) A1515,
      W. Bauer, S. Giordano and H. Hahn, J. Appl. Phys. 45 (1974) 5023,
      R.A. French, Cryogenics 8 (1968) 301,
      J. Ferreira da Silva, E.A. Burgemeister and Z. Dokoupil, Physica 41 (1969) 409.

[32] G.S. Mkrtchyan and V.V. Shmidt, Zh. Eksp. Teor. Fiz. 61 (1971) 367 and JETP 34 (1972) 195.

[33] B. Bonin and H. Safa, Supercond. Sci. Technol. 4 (1991) 257,
      C. Attanasio, L. Maritato and R. Vaglio, Phys. Rev. B43 (1991) 6128 and IEEE Trans.
      Mag. 27 (1991) 1920.

[34] T.L. Hylton, A. Kapitulnik, M.R. Beasley, J.P. Carini, L. Drabeck and G. Gruener,
      Appl. Phys. Lett. 53 (1988) 1343,
      J. Halbritter, J. Supercond. 5 (1992) 331, 8 (1995) 691 and 10 (1997) 91.

[35] D.W. Hoffman and J.A. Thornton, Thin Solid Films 40 (1977) 355 and J. Vac. Sci.
      Technol. 17 (1980) 380,
      B. Window, J. Vac. Sci. Technol. A11 (1993) 1522.

[36] W. De Sorbo, Phys. Rev. 132 (1963) 107 and 134 (1964) A1119,
      S. Giordano, H. Hahn, H.J. Halama and C. Varmazis, J. Appl. Phys. 44 (1973) 4185.

[37] C.S. Tedmon, Jr., R.M. Rose and J. Wulff, J. Appl. Phys. 36 (1965) 164,

C.S. Furtado, Cryogenics 13 (1973) 639,

C.C. Koch, J.O.Scarbrough and D.M.Kroeger, Phys.Rev.B (1974) 888,

P.Kneisel, O.Stolz and J.Halbritter, J.Appl.Phys. 45 (1974) 2296 and IEEE Trans. Nucl. Sc. 20 (1973) 63,

A. Das Gupta, W. Gey, J. Halbritter, H. Kuepfer and J.A. Yasaitis, J. Appl. Phys. 47 (1976) 2146.

[38] W. Weingarten, Proc. 7th Workshop on RF Supercond., ed. B. Bonin, Gif-sur-Yvette, France, p.129 (1995), CEA/Saclay 96-080/1.

[39] E. Mahner, private communication, unpublished.

[40] J. Shumway and S. Satpathy, Phys. Rev. B 56(1997) 103.

[41] H. H. Andersen and E. Johnson, Nucl. Inst. Meth. B106 (1995) 480 and references therein,

S.E. Donnelly, Radiat. Eff. 90 (1985) 1 and references therein,

A. vom Felde, J. Fink, Th. Mueller-Heinzerling, J. Pflueger, B. Scheerer, G. Linker and D. Kaletta, Phys. Rev. Lett. 53 (1984) 922,

A.H. Sorensen, E. Johnson, K.K. Bourdelle, A. Johansen, H.H. Andersen and L. Sarholt-Kristensen, Phil. Mag. A75 (1997) 1533,

H.H. Andersen, J. Bohr, A. Johansen, E. Johnson, L. Sarholt-Keristensen and V. Surganov, Phys. Rev. Lett. 59 (1987) 1589,

E. Johnson,E. Gerritsen, N.G. Chechenin, A. Johansen, L, Sarholt-Kristensen, H.A.A. Keetels, L. Graabaek and J. Bohr, Nucl. Inst. Meth. B39 (1989) 573,

C.J. Rossouw and S.E. Donnelly, Phys. Rev. Lett. 55 (1985) 2960,

C. Templier, H. Garem and J.P. Riviere, Phil. Mag. A53 (1986) 667,

L.S. Palatnik, A.A. Koz'ma, M.Ya. Fuks, T.I. Peregon and L.P. Tishchenko, Phys. Chem. Mech. Surfaces 4 (1982) 1171,

L.P. Tishchenko, T.I. Peregon and A.G. Koval, Phys. Chem. Mech. Surfaces 4 (1986) 870

M.P. Volkov, Yu.N. Sokurskiy, S.I. Tsypkin, V.I. Chuyev and V.N. Shiskov, Phys. Met. Metall. 59 (1985) 58.

[42] L. Ji, M.S. Rzchowski and M. Tinkham, Phys. Rev. B42 (1990) 4838.

[43] G. Song, M. Geitz, A. Abroweit and H. Zabel, Phys. Rev. B54 (1996) 14093,

Baker and H.K. Birnbaum, Acta Metallurgica, 21 (1973) 86,

T. Schober, Scripta Metallurgica 7 (1973) 1119,

J.M. Welter and F.J. Johnen, Z. Phys. B27 (1977) 227,

G.V. Khaldeev and V.K. Gogel, Usp. Khimii 56 (1987) 1057, english translation in Russian Chem. Rev. 56 (1987) 605,

R. Hempelmann, J. Less Comm. Metals 101 (1984) 69,

G.C. Rauch, R.M. Rose and J. Wulff, J. Less Comm. Metals 8 (1965) 99,

J. Steiger, S. Blaesser and A. Weidinger, Phys. Rev. B49 (1994) 5570,

B. Roux, H. Jaffrezic, A. Chevarier, N. Chevarier and M.T. Magda, Phys. Rev. B52 (1995) 4162.

[44] B. Bonin and R.W. Roeth, Proc. 5th Workshop on RF Supercond., ed. D. Proch, DESY, Hamburg, Germany, p.210 (1991), DESY-M-92-01 and references therein,

S. Isagawa, J. Appl. Phys. 51 (1980) 4460 and 6010.

[45] M. Peiniger, M. Hein, N. Klein, G. Mueller, H. Piel and P. Thuens, Proc. 3rd Workshop RF Supercond., ANL-PHY-88-1- II, 503, 1988.

[46] G. Arnolds-Mayer and W. Weingarten, IEEE Trans. Mag. 23 (1987) 1620,

Ph. Bernard, D. Bloess, T. Flynn, C. Hauviller, W. Weingarten, P. Bosland and J. Martignac, Proc. 1992 Eur. Part. Acc. Conf., ed. E.H. Henke *et al.*, Ed. Frontieres, p.1269,

W. Weingarten, Part. Acc. 53 (1996) 199 and references therein.

Table 1. Properties of the copper substrates

Type	Thermal conductivity (4.2 K) [W/mK]	RRR (4.2 K)	O content [ppm weight]	Total purity [%]	Grain size [μm]	Roughness [μm]	Hardness $HV_{0.2}$
Hydroformed	550 ± 50	400 ± 40	0.9	99.998	50 to 100 (equiaxed)	1	100
Spun	540 ± 70	77 ± 8	0.7	99.998	100 x 10 (elongated)	0.2	98
Electroformed	2900 ± 400	890 ± 50	0.8	99.998	50 to 100 (equiaxed)	0.35	49

Table 2. RRR and gas concentrations

Discharge gas	RRR	Gas content [ppm]
100% Xe (600 V)	23 ± 3	10
100% Kr (600 V)	27 ± 4	10
100% Ar	18 ± 2	350
80% Ar/20% Ne	15 ± 2	1300
50% Ar/50% Ne	13 ± 2	3300
33% Ar/67% Ne	10 ± 2	5200
20% Ar/80% Ne	9 ± 2	8500
10% Ar/90% Ne	6 ± 1	17000
100% Ne	3 ± 1	27000

Table 3. Summary list of variables.

Films grown on oxidised copper								
Discharge gas	T_c [K]	λ_{rel}	H_{rel}	R_{BCS}^0 [nΩ]	$\tilde{\Delta}$ [K]	R_{fl}^0 [nΩ/G]	R_{fl}^1 [nΩ/G/mT]	k_{fl}
100% Xe	9.48±0.03	1.62±0.12	0.66±0.03	438±12	18.7±0.5	5.04±0.08	0.99±0.09	2.60±0.12
100% Kr	9.49±0.03	1.49±0.11	0.65±0.03	400±7	19.0±0.4	2.94±0.05	0.55±0.02	2.64±0.10
100% Ar	9.50±0.03	1.56±0.05	0.65±0.03	401±3	19.4±0.1	5.05±0.02	1.09±0.04	2.72±0.04
80% Ar 20% Ne	9.51±0.03	1.85±0.13	0.63±0.05	384±6	18.3±0.6	4.41±0.14	1.07±0.03	2.53±0.06
50% Ar 50% Ne	9.53±0.03	2.13±0.23	0.56±0.03	406±12	18.6±0.6	6.20±0.30	2.17±0.09	2.60±0.20
30% Ar 70% Ne	9.50±0.03	2.37±0.19	0.52±0.03	444±8	19.1±0.6	6.30±0.40	3.40±0.20	2.28±0.05
10% Ar 90% Ne	9.13±0.03	3.16±0.31	0.51±0.03	655±15	18.5±0.5	21.20±0.50	21.10±0.40	1.83±0.10
Films grown on oxide free copper								
100% Xe	9.35±0.03	1.24±0.10	0.52±0.03	530±10	18.2±0.6	87.00±3.00	4.90±0.30	1.85±0.06
100% Kr	9.31±0.03	1.02±0.07	0.52±0.03	554±20	17.3±0.5	91.60±0.74	3.70±0.28	2.06±0.17
100% Ar	9.42±0.03	1.14±0.08	0.63±0.03	464±11	18.4±0.3	50.54±0.39	5.10±0.48	1.89±0.05
80% Ar 20% Ne	9.53±0.03	1.29±0.19	0.53±0.03	383±10	19.4±0.9	14.80±0.30	2.68±0.04	2.02±0.05
67% Ar 33% Ne	9.56±0.03	1.41±0.19	0.54±0.03	365±5	18.9±0.6	6.90±0.40	1.91±0.06	2.75±0.10
50% Ar 50% N	9.50±0.03	1.99±0.17	0.35±0.02	420±6	19.5±0.5	4.70±0.30	2.12±0.05	2.89±0.08
20% Ar 80% Ne	9.41±0.03	2.81±0.22	0.37±0.02	511±8	18.6±0.5	8.30±0.57	5.72±0.17	2.44±0.05
Bulk niobium								
---	9.28±0.03	1.05±0.05	0.94±0.05	926±23	18.7±0.3	102.2±1.1	0.75±0.40	1.40±0.04

Figure captions

Fig. 1. Geometry of the resonators used in the experiment and distribution of the amplitudes of the electric and magnetic fields on the cavity surface.

Fig. 2. Schematic drawing of the single-cathode coating system.

Fig. 3. A typical set of Q *vs* E_{acc} measurements. The upper and lower branches are isotherms taken at 1.7 K and 4.2 K respectively. The points in-between were taken while pumping on the cryostat.

Fig. 4. Examples of measurements of the trapping efficiency and of the critical temperature. The magnetic field H measured in one of the Hall probes is displayed as a function of temperature for zero field cooled (squares) and field cooled (circles) data respectively

a) A typical film with full flux trapping,

b) A heat-treated bulk niobium cavity with incomplete flux trapping.

Fig. 5. Temperature dependence of the penetration depth. The quantity $g(t) = (1\text{-}t)\ dF/dt$ (normalized at $t = 0.9$) is displayed as a function of $= T/T_c$. The full line is the prediction of the two-fluid model, the dotted line is the result of a linear fit to the logarithm of the quantity plotted.

Fig. 6. A typical H_p measurement. The measured surface resistance R_s is displayed as a function of the current I in the superconducting coil. The knee of the curve, obtained from a linear fit to lnR_s *vs* I, defines H_p.

Fig. 7. Dependence of R_{BCS} (4.2 K) on H_{rf}. Error bars include the effect of the spread between different films. The line is the result of a quadratic fit.

Fig. 8. Isothermal H_{rf} scans measured on a particular film. R_{BCS} (T) is plotted as a function of H_{rf} for T 4.2 K, 3.9 K, 3.4 K, 3.0 K, 2.5 K, 2.4 K and 2.1 K (from top to bottom). The lines represent a same H_{rf} dependence (up to a factor) for all values of T.

Fig. 9. Temperature dependence of $r = R_{BCS}$ (T)/R_{BCS} (4.2 K). Error bars include the effect of the spread between different films. The line corresponds to Relation 5 with $\tilde{\Delta} = 19.6$ K as obtained from a fit to the data (see Fig. 10).

Fig. 10. The energy gap evaluated from the data at different temperatures (see text). The line $\tilde{\Delta} = 19.6 \pm 0.2$ K is the best fit to the data.

Fig. 11. The dependence of R_{BCS} on $\lambda_{rel}^2 = 1+(\pi/2)\ \xi_0/l$ for different cavities (see Table 3). The line is the result of a BCS calculation [10] using $\lambda_L(0) = 27$nm, $\xi_0 = 33$ nm and $\alpha = 1.87$. The experimental data are scaled to $T_c = 9.54$ K (see text).

Fig. 12. Consistency check for the $\lambda_L(0)$ measurements. The horizontal band indicates the minimal measured R_{BCS} value (when l is varied). Its intersection with the oblique line (BCS calculation [10]) localises $\lambda_L(0)$ in the lower vertical band (25 to 29 nm). The upper vertical band (29 to 37 nm) is deduced from direct penetration depth measurements using the temperature dependence of the resonance frequency. While there is no overlap, both sets of data are consistent with $\lambda_L(0) = 29 \pm 3$ nm.

Fig. 13. Dependence of $R_{fl}(1.7$ K$)$,

a) on H_{rf} for $H_{ext} = 3.52$ G,

b) on H_{ext} for $H_{rf} = 3.4 \pm 1.1$ mT.

Fig. 14. The dependence on H_{rf} of R_{fl} (1.7 K)/H_{ext} . The line is a fit to the data of the form $R^0_{fl} + R^1_{fl}\ H_{rf}$.

Fig. 15. The dependence on H_{ext} of $R_{fl}(1.7\ \text{K})/(R^0_{fl} + R^1_{fl}\ H_{rf})$.

Fig. 16. An extreme case of high H_{thr} film. The value of R_{fl} (1.7 K), extrapolated to $H_{rf} = 0$, is shown as a function of H_{ext}. Above threshold ($H_{thr} = 5.7$ G), R_{fl} (1.7 K) increases in proportion to $H_{ext} - H_{thr}$ at approximately the same rate as for good quality films.

Fig. 17. The temperature dependence of R_{fl} (T)/R_{fl} (1.7 K). The point at 4.2 K (small error bar) corresponds to $k_{fl} = 2.72$.

Fig. 18. The H_{rf} dependence of R_{res} for cavities chosen among those having the lower R_{res} values limited to the H_{rf} range below field emission.
a, b, c) Standard films (see Section 4),
d) A film grown with krypton as discharge gas (see Section 5.2),
e, f) Heat-treated bulk niobium cavities, spun (e) and deep-drawn (f).

Fig. 19. The dependence of H_{rel}^2 on $\lambda_{rel}^2 = 1 + (\pi/2)\ \xi_0/l$. The data include bulk cavities (triangles), films grown on oxidised copper or on titanium (squares) and films grown on oxide free copper (circles). The lines are drawn to illustrate the strong H_{rel} reduction observed in the latter case.

Fig. 20. The values of l/ξ_0 measured on resonators from $\lambda_{rel}^2 = 1 + (\pi/2)\ (\xi_0/l)$ (circles) and measured on samples from *RRR* data (triangles). The films were grown in an argon/neon mixture. The neon fraction in the mixture is used as abscissa. The line is the result of a global fit to the data.

Fig. 21. The dependence of the fluxon induced losses, R^0_{fl} (a) and R^1_{fl} (b), on λ_{rel}^2 (symbols as for Fig. 19).

Fig. 22. Fluxon induced losses: the distribution of measured losses in the R^1_{fl} *vs* R^0_{fl} plane. Symbols are as for Fig. 19. Krypton data (on oxidised copper substrate) are labelled with full symbols.

Fig. 23. The dependence of k_{fl} on λ_{rel}^2. Symbols are as for Fig. 19.

Fig. 24. The dependence of $\tilde{\alpha} = \tilde{\Delta}/T_c$ on critical temperature for five categories of superconductors: bulk (triangle), films grown on clean copper (circle), films grown on baked-out copper (cross), films grown on re-oxidised copper (diamond) and films grown on oxidised copper or titanium (square).

Fig. 25. Schematic geometry of fluxon dynamics (see text).

Fig. 26. The Bragg spectra measured with a monochromatic incident beam (K_α of Cu) for films grown on oxidised copper (top) and on oxide free copper (bottom). Niobium planes are labelled as (hkl) and copper planes as {hkl}. A small residual K_β unfiltered component is still visible.

Fig. 1

Cooling

OUT   IN

Ceramic insulator

Magnet

RF Cavity

Plasma

Nb Cathode

Dust-free valve

L.P. Gauge
H.P. Gauge

Argon

R G A

Main valve

Diaphragm

Main Pump

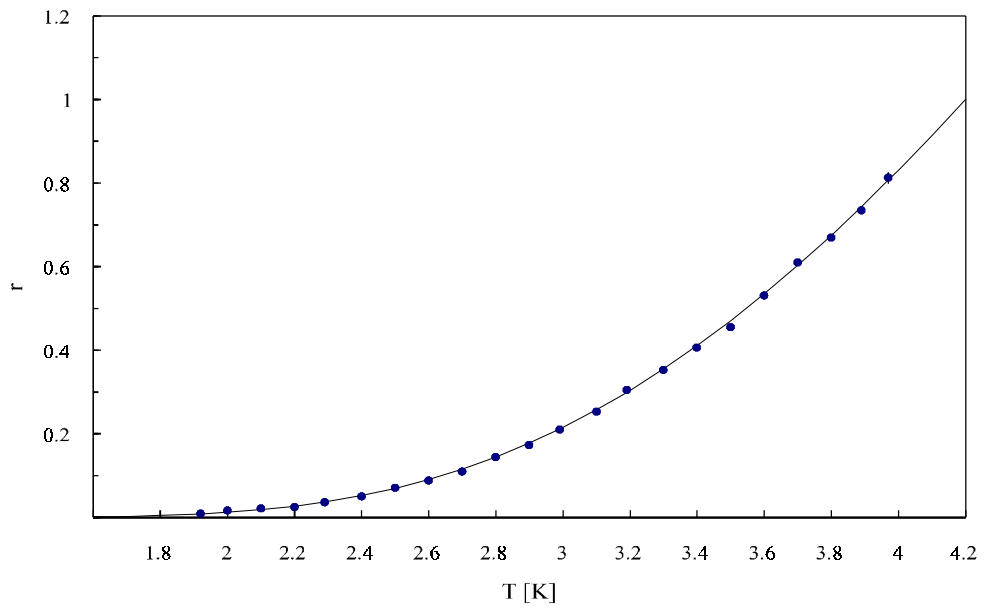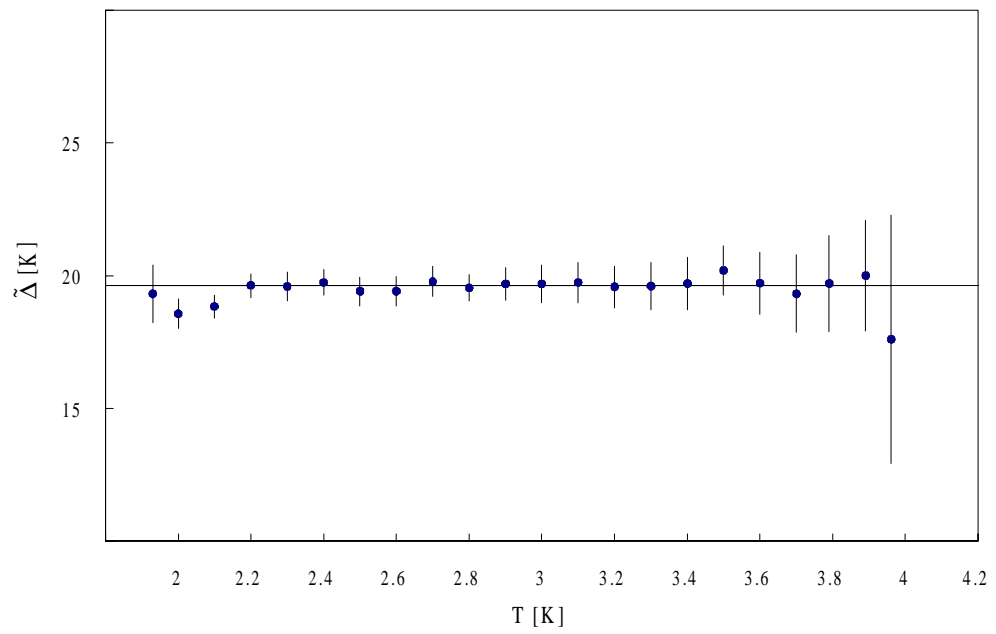Differential
pumping
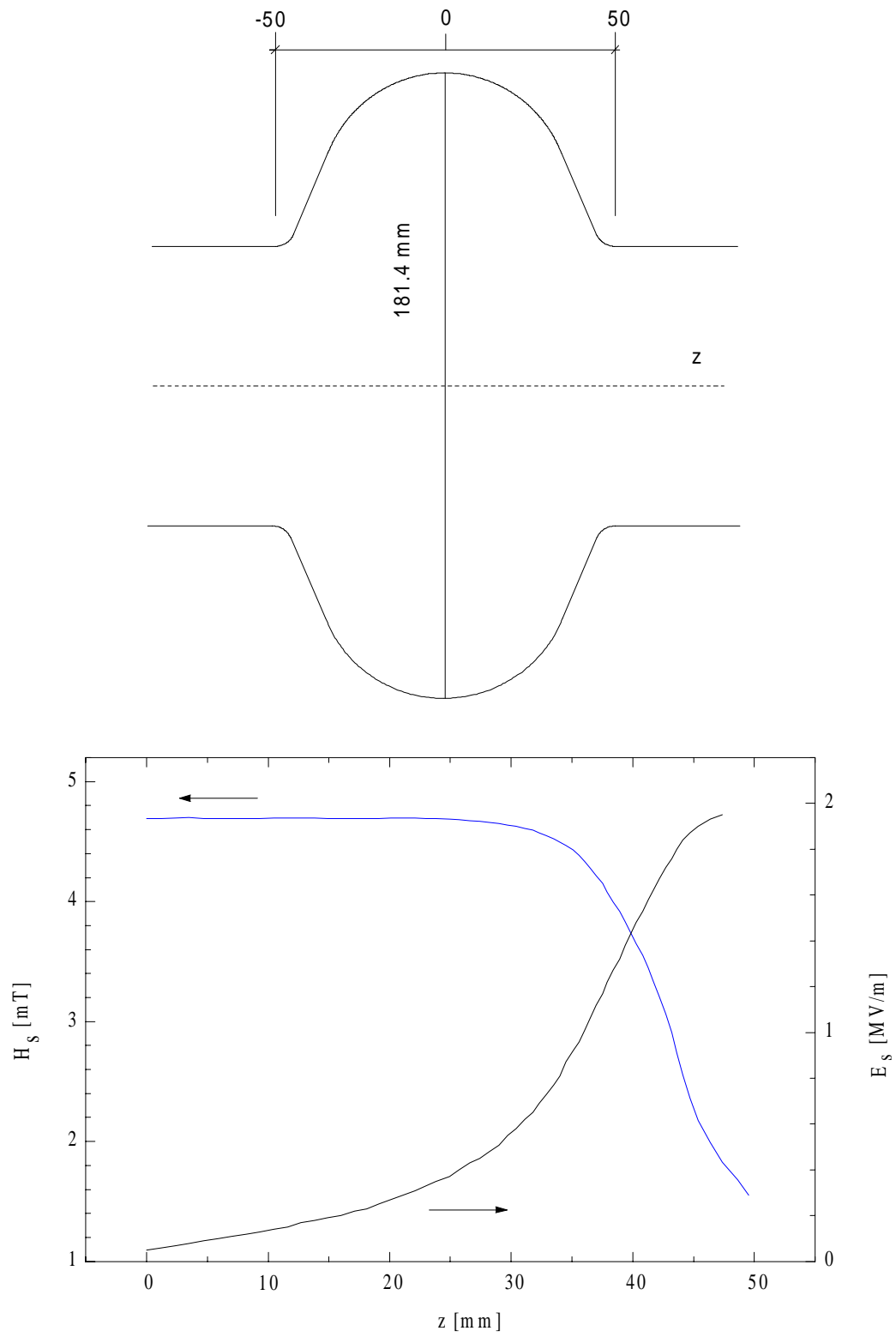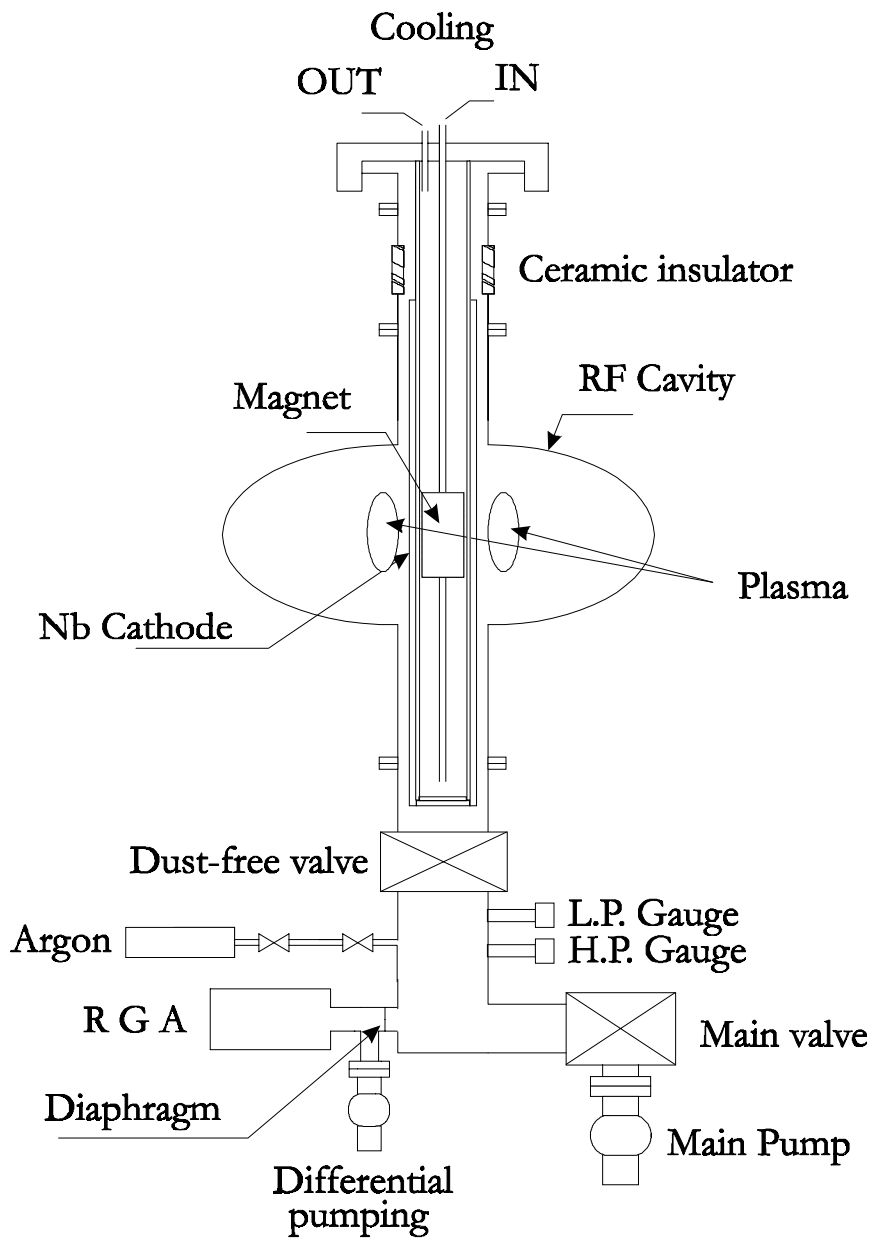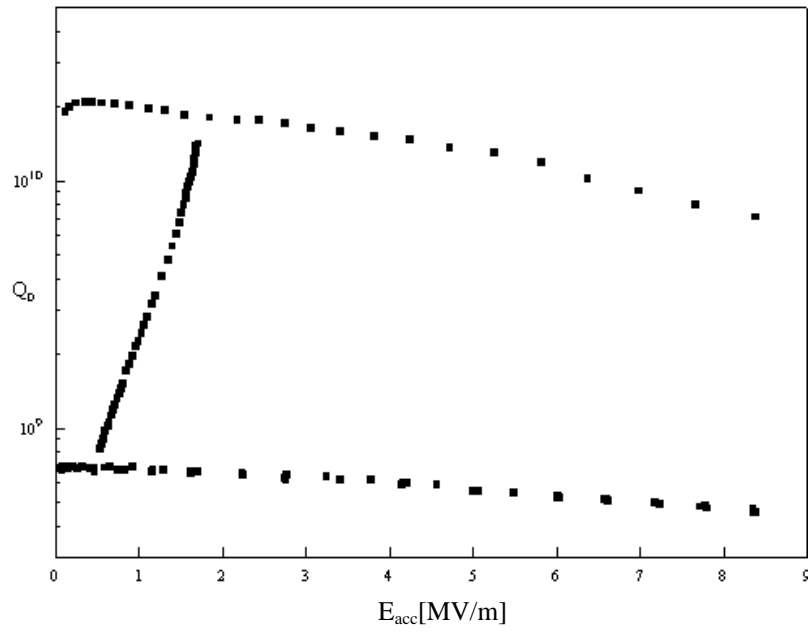
Fig. 2
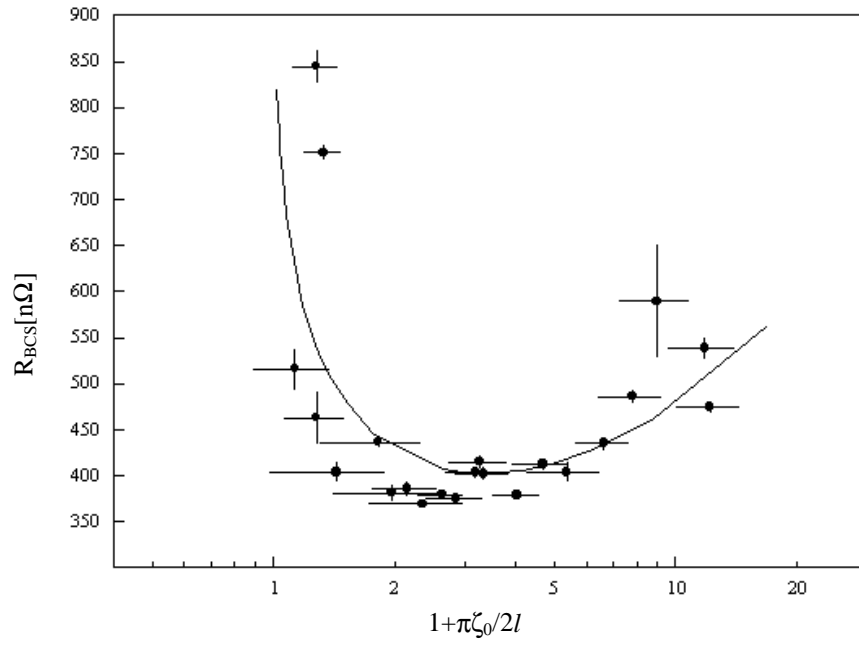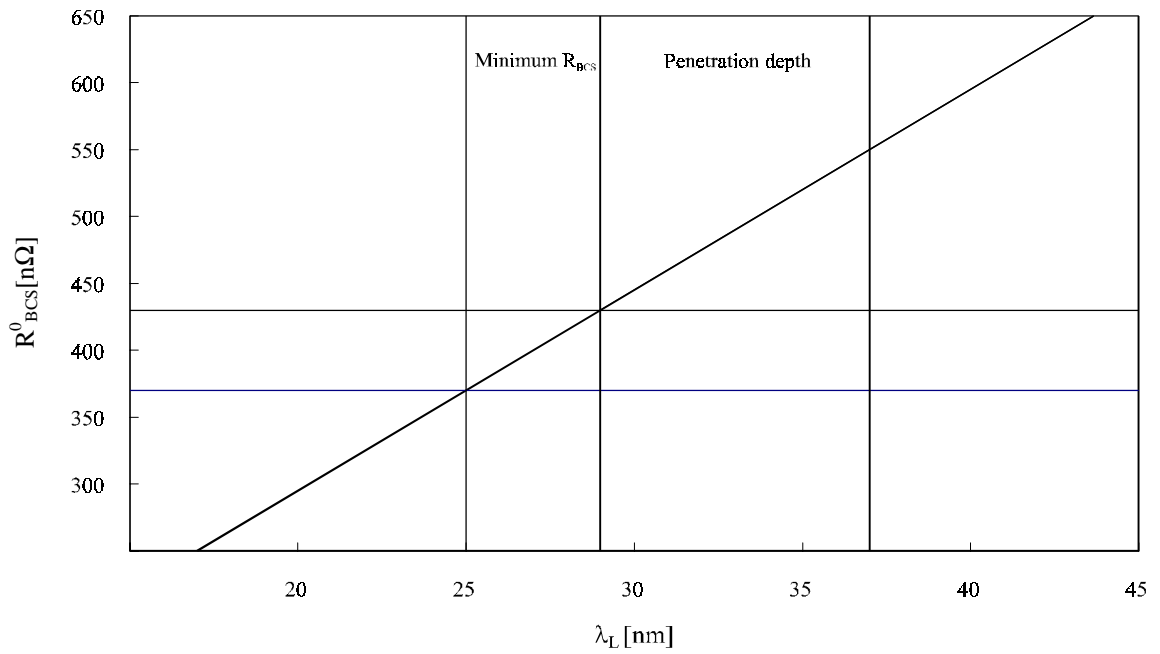
Fig. 3
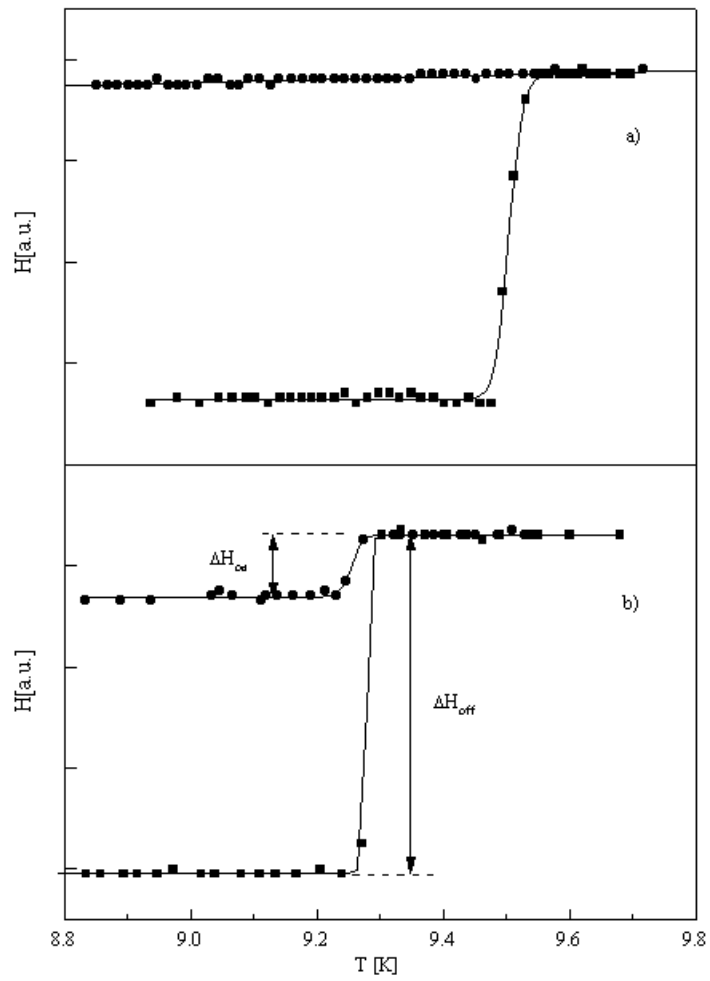
Fig. 4
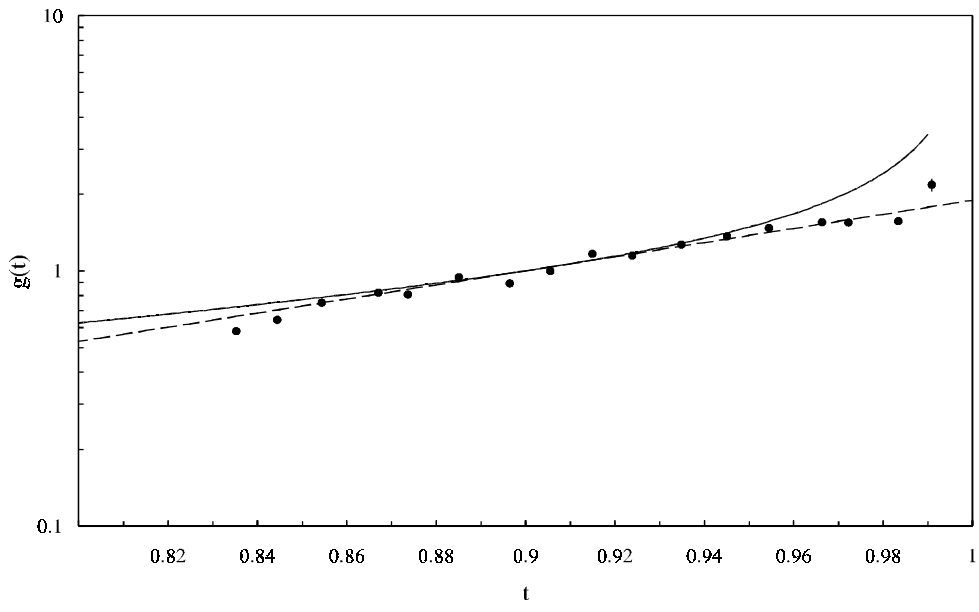
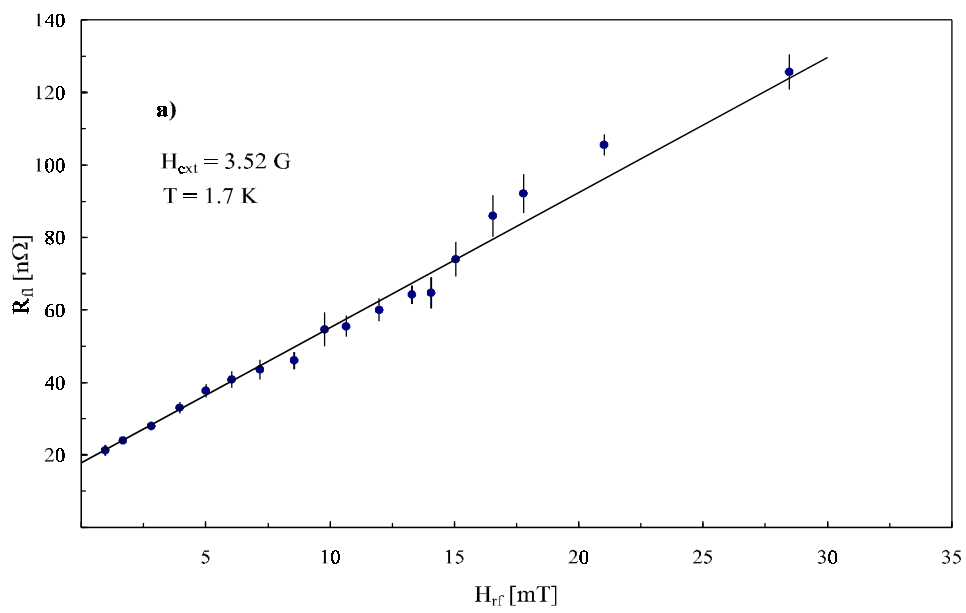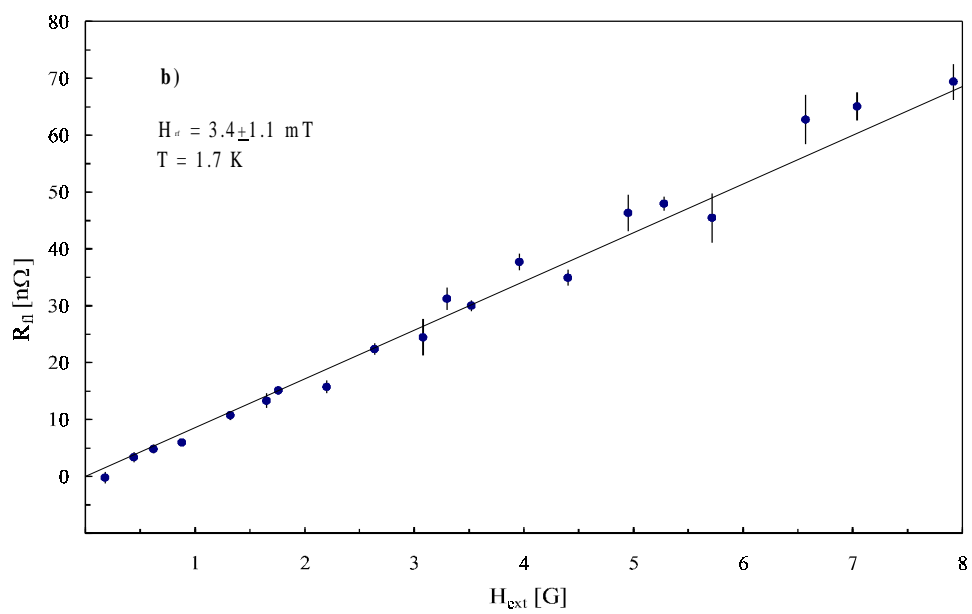**Fig. 5**
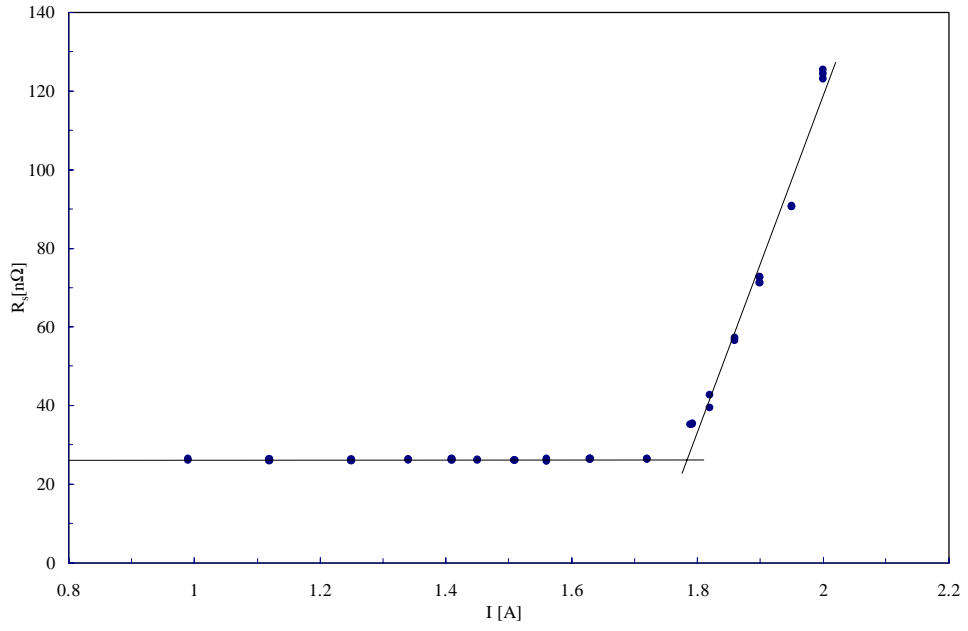
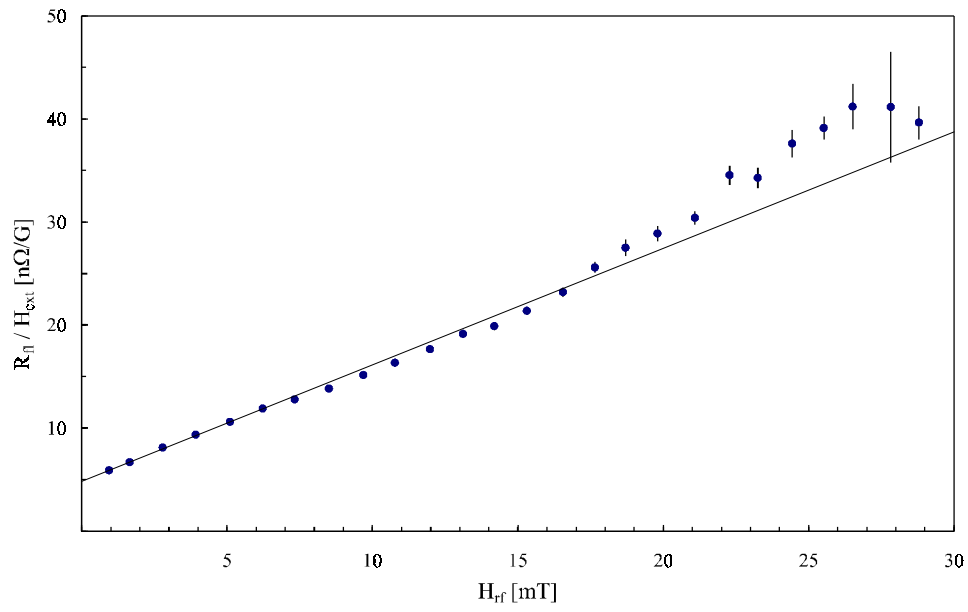**Fig. 6**
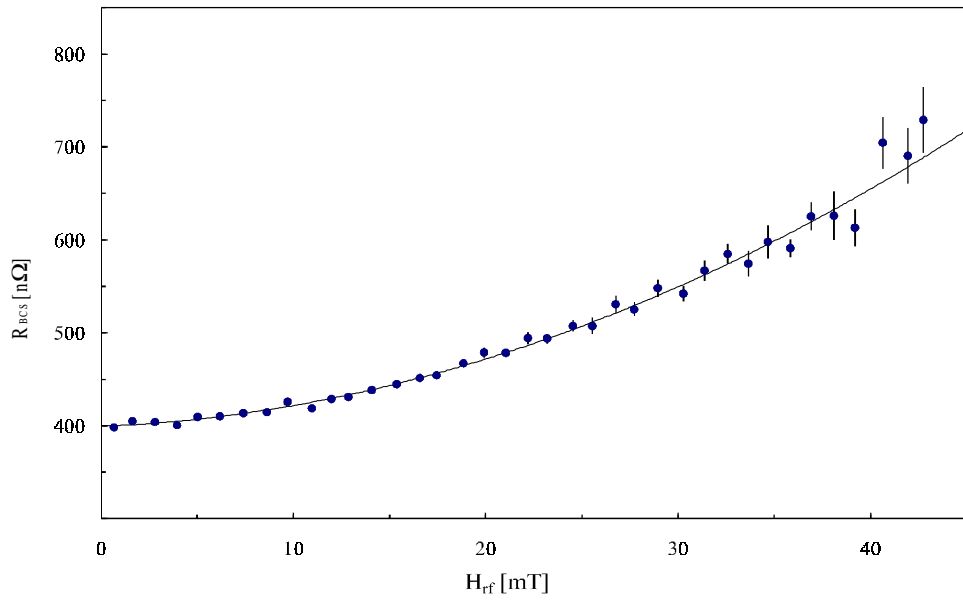
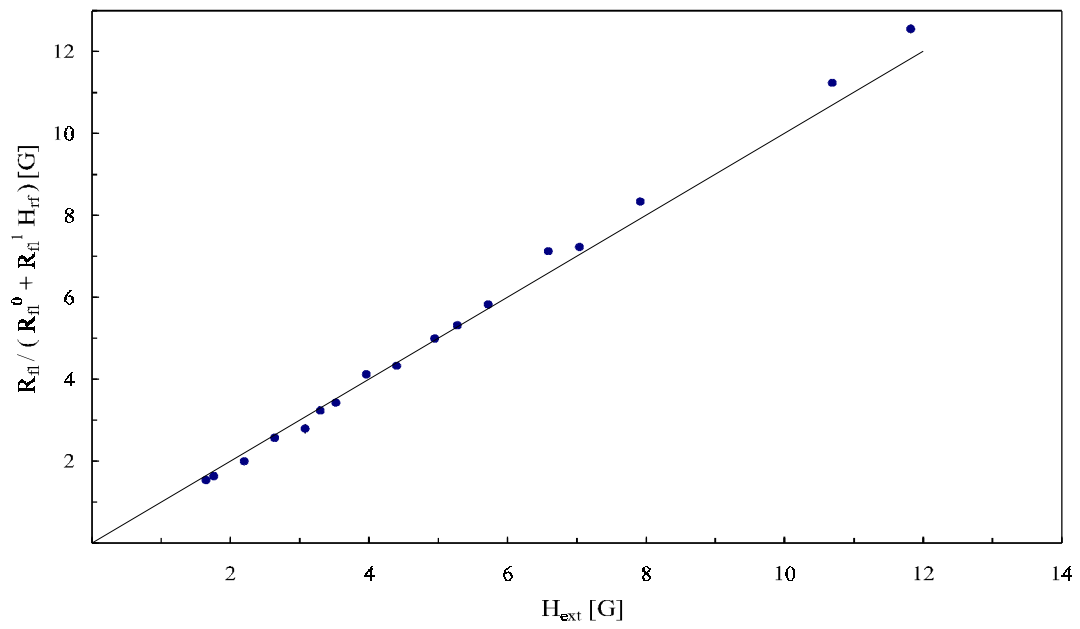**Fig. 7**
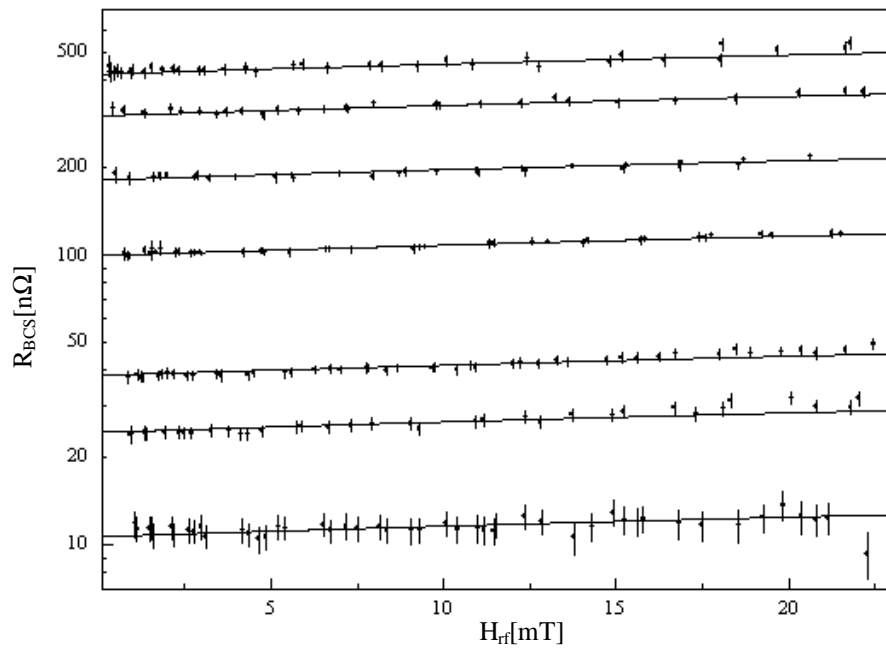
Fig. 8

Fig. 9
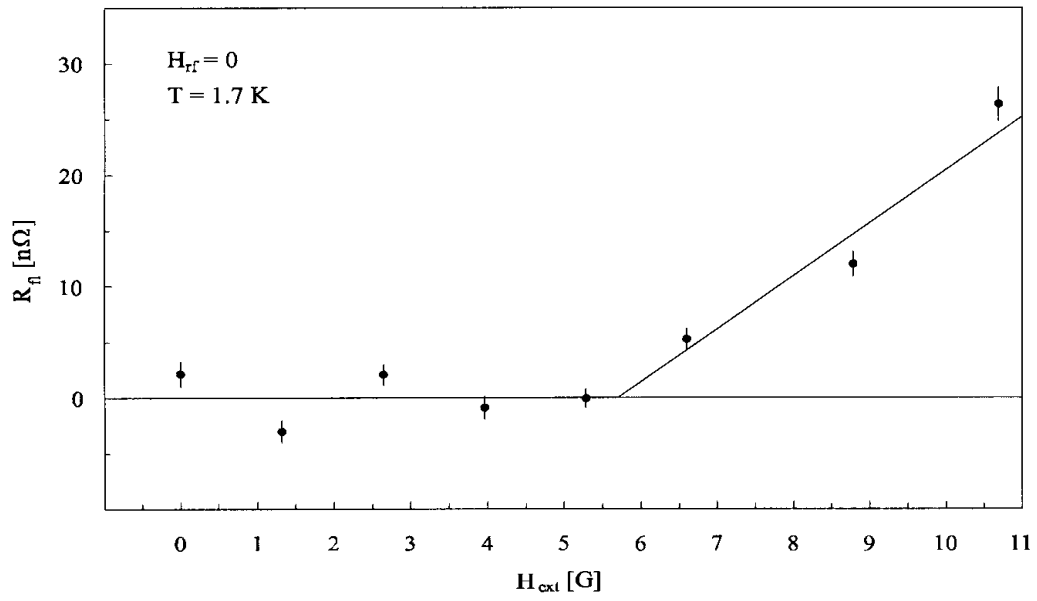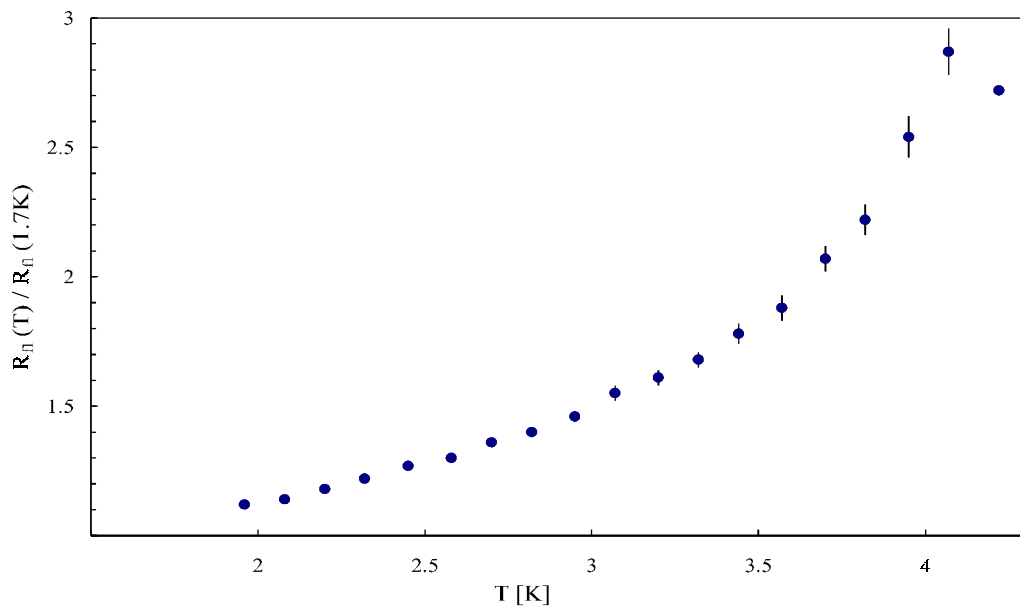

Fig. 10
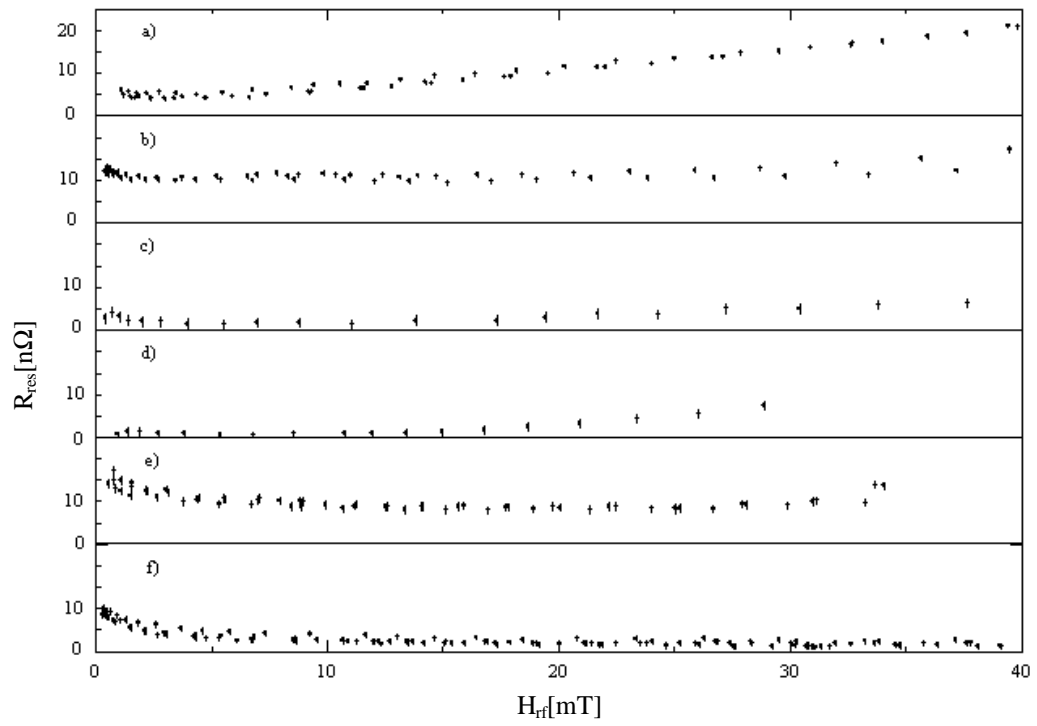
Fig. 11
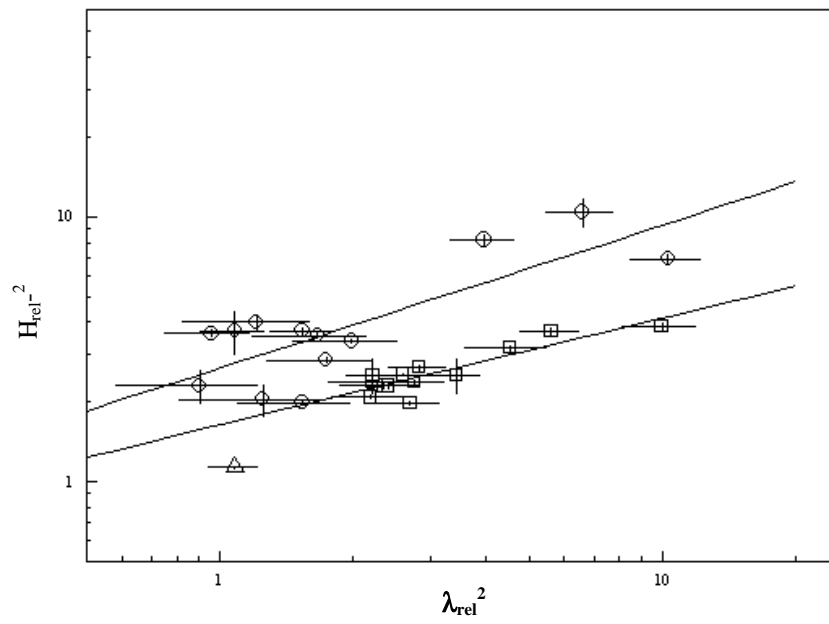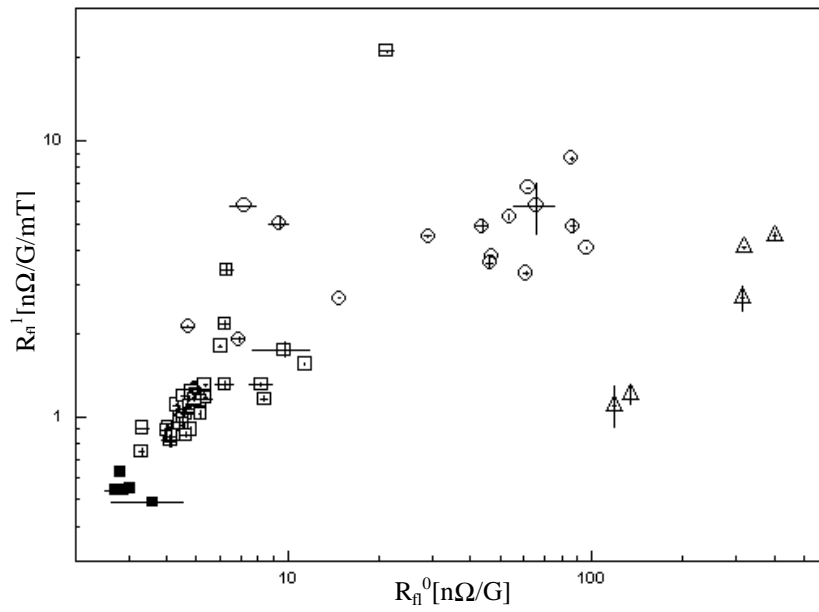

Fig. 12

Fig. 13 a)

Fig. 13 b)

Fig. 14
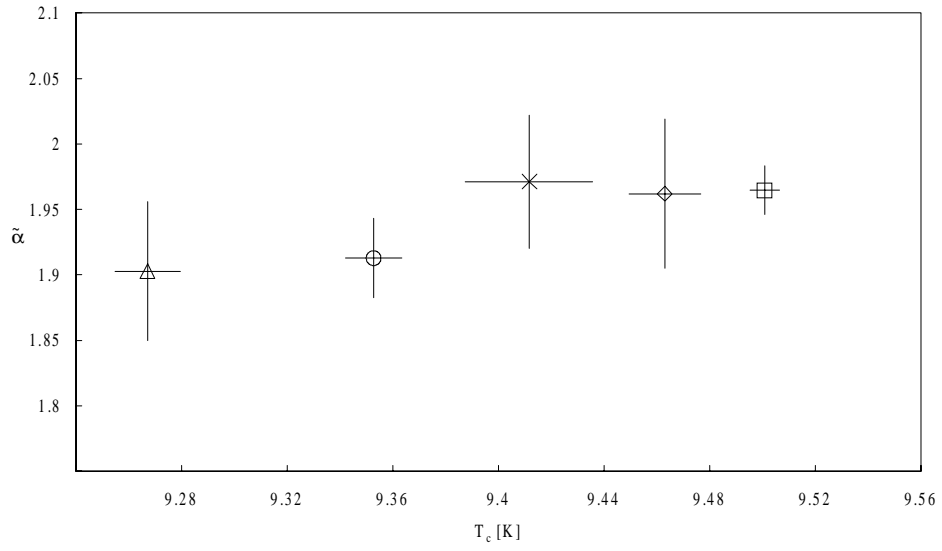

Fig. 15

Fig. 16

Fig. 17

Fig. 18

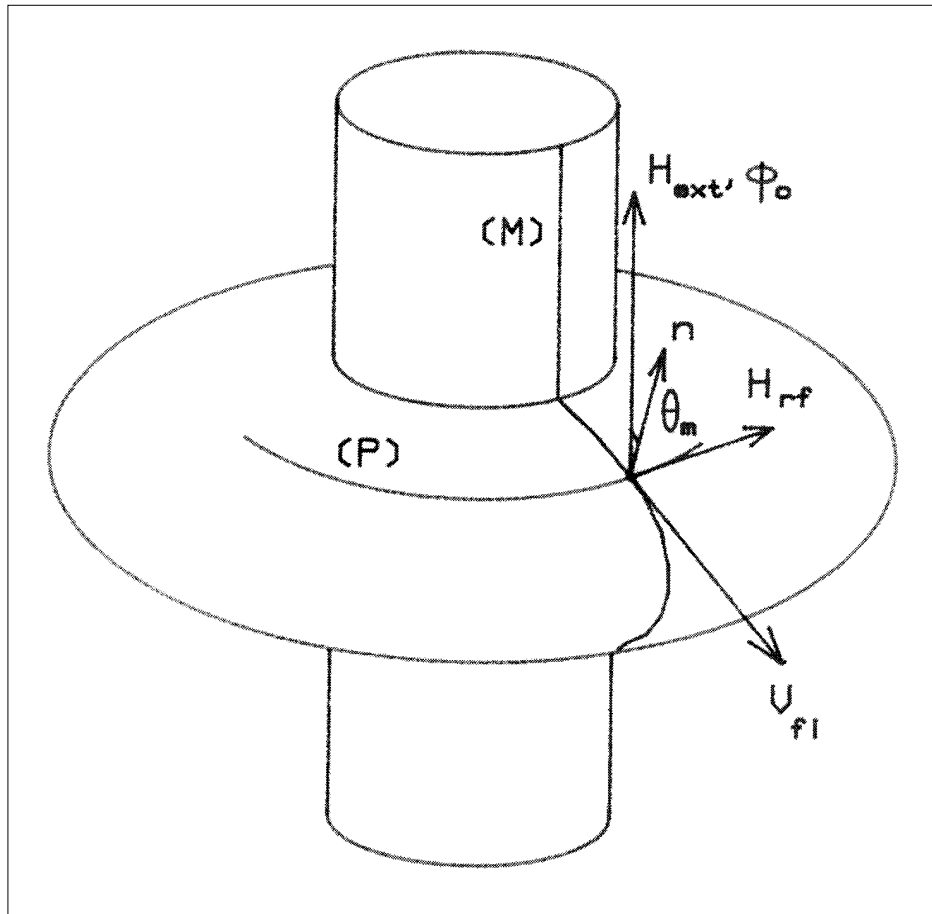**Fig. 19**

Fig. 20
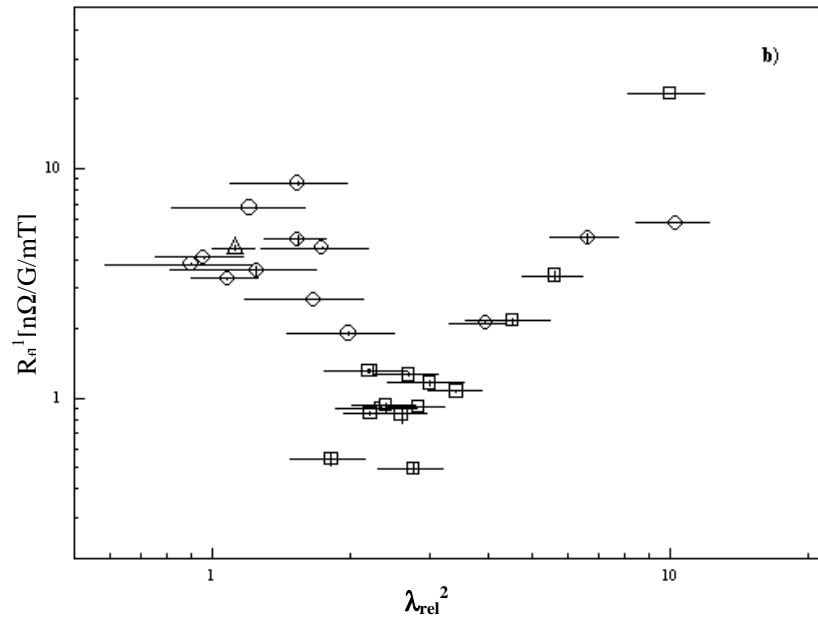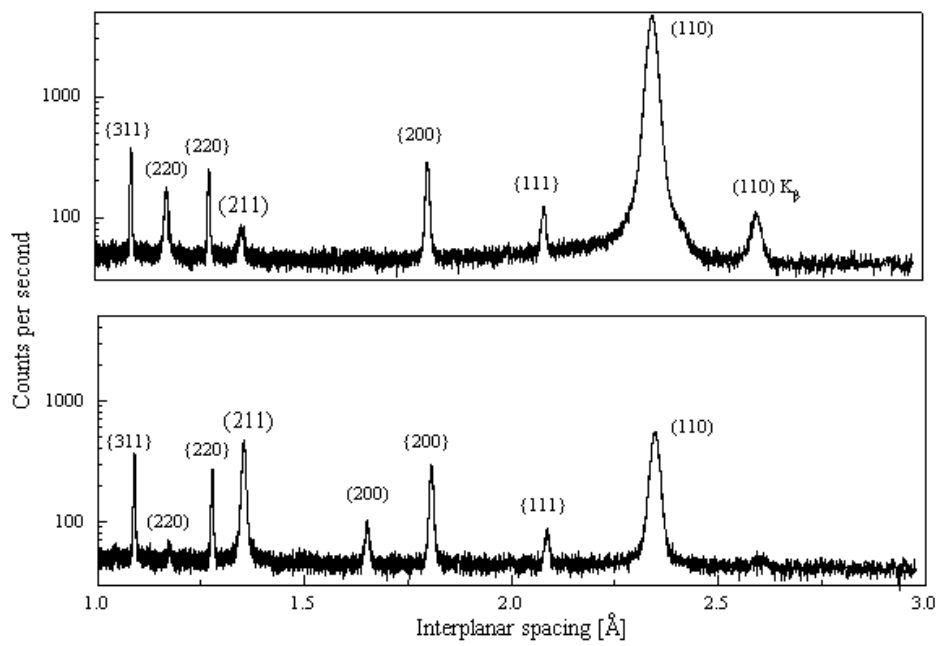

Fig. 21 a)

Fig. 21 b)

Fig. 22

Fig. 23

Fig. 24

Fig. 25

Fig. 26